

n:m Phase-Locking of Heterogeneous and Strongly Coupled Oscillators

Youngmin Park^{*1}

¹*Department of Mathematics, University of Florida, Gainesville, FL 32611*

Abstract

We introduce a scalar reduction method beyond weak perturbations for forced or coupled systems to determine the existence and stability of $n:m$ phase-locked states. We consider various biologically relevant oscillators including the nonradial isochron clock and thalamic neural oscillators. The proposed scalar reduction successfully captures the emergence and disappearance of phase-locked states as a function of coupling strength and heterogeneity. We find that even small amounts of heterogeneity (often orders of magnitude smaller than the coupling strength) can significantly alter phase-locked states. The proposed method is a straightforward means to both reduce and analyze potentially high-dimensional systems of coupled oscillators in more biologically realistic settings.

1 Introduction

Coupled oscillators are ubiquitous in natural and physical systems. Pacemaker neurons coordinate to generate collective rhythms in the nervous system across countless species of vertebrates and invertebrates [3, 50, 15, 21, 51]. The walking patterns of crowds on bridges may elicit a resonance response, where the bridge acts as a mechanical coupling between individuals [41, 30]. Chemical preparations such as the famed Belousov–Zhabotinsky reaction exhibit spatio-temporal patterns through diffusive coupling [16, 6]. In particular, $n:m$ phase-locking, where one coupled oscillator traverses n periods in the same time that the other traverses m periods, is a natural feature of physical systems such as microelectromechanical system (MEMS) oscillators [2], pulse-coupled cardiac pacemakers [27], and Belousov–Zhabotinsky chemical oscillators with asymmetric coupling [13].

Homogeneity and *symmetry* are common assumptions in the study of coupled oscillators that turn relatively complex models and behaviors into amenable forms for mathematical analysis. The Kuramoto oscillator is a classic example upon which significant progress has been made, such as the celebrated Ott–Antonsen ansatz [30], and recent fashionable works on N -body interactions on simplicial complexes [1]. Homogeneity and symmetry also allow detailed analytical studies of the existence and stability of $n:m$ phase-locked states for even strong coupling strengths and high-dimensional oscillators, e.g., through the application of group theory (specifically H/K theory) [12]

^{*}Corresponding author park.y@ufl.edu

and firing time maps [4]. It is also common to use particular models that are analytically tractable, like the Van der Pol oscillator [2], circle map-like systems [10], and the Rössler oscillator [5].

However, in biological systems, *heterogeneity* is an inescapable feature that alters the behavior of coupled oscillators in the physical world. Experimental preparations of chemical oscillators with only 3% variation in intrinsic frequencies disrupt the existence and stability of phase-locked states predicted using H/K theory [14]. Introducing heterogeneity in ecosystem models has been shown to have significant effects on phase dynamics [11, 26]. Biological neural networks, such as brains, do not consist of homogeneous neurons; instead, exhibiting high degrees of heterogeneity [40, 42]. Heterogeneity may even be a necessary feature of robust brain function [17]. The ubiquity of heterogeneity in nature warrants exploration in this direction. However, general phase-reduction methods that incorporate heterogeneity are relatively lacking.

We introduce a method to reduce a pair of $n:m$ coupled heterogeneous oscillators to relatively tractable equations in a manner similar to classic weak coupling theory (see [16, 9, 38, 32] for introductory texts on the theory of weakly coupled oscillators). The proposed method uses a combination of phase and isostable coordinates employed in recent works [48, 45, 33, 34, 28]. The proposed method does not require oscillators to be strongly attracting (such as in many phase-based approaches, e.g., [4]), nor does it require perturbed solutions to be near the unperturbed limit cycle.

This paper is organized as follows. In Section 2, we briefly discuss the phase-isostable reduction and establish standard notation we will use throughout this paper. In Section 3, we introduce the assumptions on the types of vector fields amenable to the reduction, then derive the phase-isostable reduction for $n:m$ coupling. We then apply this reduction to a forced nonradial isochron clock in Section 4.1.1, a forced thalamic model in Section 4.1.2, and to a pair of coupled thalamic neurons in Section 4.2.1. We conclude with a discussion in Section 5.

2 Background for the Phase-Isostable Reduction

2.1 Phase Reduction

Consider a general dynamical system,

$$\frac{dX}{dt} = F(X) + \varepsilon U(X, t), \quad (1)$$

where $X \in \mathbb{R}^n$ is the vector of state variables, $F : \mathbb{R}^n \rightarrow \mathbb{R}^n$ is a smooth vector field, and $U(X, t) \in \mathbb{R}^n$ is some additive input function. The function U could represent an endogenous or exogenous forcing function, or a reciprocally coupled oscillator.

Let $\Gamma(t)$ be a stable T -periodic limit cycle satisfying (1) for $\varepsilon = 0$, which persists for some range of $\varepsilon \neq 0$. The classic theory of weakly coupled (or weakly forced) oscillators seeks to understand how *weak* perturbations, $0 < \varepsilon \ll 1$, affect the *timing* of oscillators. In the case of two oscillators and a given state variable, this timing is intuitively defined as the time difference when the oscillators cross a Poincaré section. Will they synchronize, i.e., will the time difference converge to zero? Or will they exhibit some other *phase-locked* behavior, where the time difference converges to some nonzero constant?

This time difference can be quantified by computing the phase of each oscillator, then taking the *phase difference*. To compute an oscillator's phase, we transform (1) to a scalar variable, where the limit cycle Γ is associated with values on the unit circle, $\theta \in$

$[0, 2\pi)$ (modulo 2π)¹. In the absence of coupling or forcing, $\varepsilon = 0$, it is straightforward to extend the idea of phase to the basin of attraction such that manifolds of initial conditions exhibit the same phase (isochrons) with constant phase advance,

$$\frac{d\theta}{dt} = 1.$$

Then, following the classic work of Kuramoto [16], we invoke the chain rule to derive the phase equation,

$$\begin{aligned} \frac{d\theta}{dt} &= \nabla\theta \cdot \frac{dX}{dt} \\ &= \nabla\theta \cdot F(X) + \varepsilon \nabla\theta \cdot U(X, t) \\ &= 1 + \varepsilon Z(\theta) \cdot U(X, t). \end{aligned} \tag{2}$$

The first term of the last line follows from our choice of $d\theta/dt = 1$ (literally, the directional derivative of the isochron in the direction of the vector field is always constant), and the second term is a simple relabeling of $\nabla\theta$ evaluated on the limit cycle, $Z(\theta) \equiv \nabla\theta|_{\Gamma}(\theta)$.

Equation (2) is an elegant scalar transformation of the limit cycle Γ , where the order ε term quantifies how incoming perturbations alter the constant phase advance of the unperturbed oscillator. Equation (2) is the first of two components of the phase-isostable reduction to be used in this paper.

2.2 Isostable Coordinate

While the phase reduction (2) has long been an exceptionally useful means to understand the existence and stability of phase-locked states [9, 32, 29], it requires that the limit cycle Γ is strongly attracting. In other words, perturbed solutions must return to the limit cycle within a single period for the phase reduction to be accurate. Thus, a natural limitation arises when a perturbed solution X takes multiple periods to decay back to the unperturbed limit cycle solution Γ . Such instances occur naturally with either strong perturbations or weakly attracting limit cycles [49]. Of the many methods at our disposal to address this limitation [49, 36, 43, 47, 39], we choose to augment our phase variable with *isostable coordinates* – coordinates that are defined as the level sets of the slowest decaying modes of the Koopman operator [23, 25]. We describe a more intuitive definition below, which closely follows [49, 45, 34].

Let $U(X, t) = 0$ and define $\Delta X = X - \Gamma(\theta)$. Then, to a linear approximation, our original system (1) becomes,

$$\Delta \dot{X} = J(t) \Delta X, \tag{3}$$

where $J(t)$ is the Jacobian evaluated at $\Gamma(\theta(t))$. Notice that (3) a linear system with time-varying coefficients that are T -periodic. Let Φ be the fundamental matrix, i.e., $\Delta X(T) = \Phi \Delta X(0)$ with initial condition $\theta(X(0)) \approx 0$, and let w_j, v_j , and λ_j be left eigenvectors, right eigenvectors, and associated eigenvalues, of Φ , respectively. Floquet exponents may be obtained using $\kappa_j = \log(\lambda_j)/T$, and we may sort them without loss of generality, such that κ_1 is the slowest decaying nonzero Floquet exponent. If κ_1 is unique, an associated isostable coordinate can be defined in the basin of attraction of the limit cycle [46]:

$$\psi_1(X) = \lim_{k \rightarrow \infty} (w_1^\top (\eta(t_\Gamma^k, X) - \Gamma_0) \exp(-\kappa_1 t_\Gamma^k)), \tag{4}$$

¹The phase variable θ is also often taken to be in the range $[0, 1)$ or $[0, T)$. In this work, we assume $T = 2\pi$ without loss of generality.

where t_{Γ}^k denotes the time of the k th stroboscopic transversal of the $\theta = 0$ isochron, $\eta(t, X)$ denotes the unperturbed flow of the vector field that takes $X(0)$ to $X(t)$, Γ_0 denotes the intersection between the periodic orbit and the $\theta = 0$ isochron, and \top denotes the transpose. The isostable coordinate (4) gives a sense of the distance from the periodic orbit, with greater values of $|\psi_1(X)|$ corresponding to states that will take longer to approach the periodic orbit². Using Equation (4), it is possible to show directly that when $U(X, t) = 0$,

$$\frac{d\psi_1}{dt} = \kappa_1 \psi_1 \quad (5)$$

in the basin of attraction of the limit cycle [46]. Intuitively, the amplitude ψ_1 will decay exponentially towards the limit cycle, and if κ_1 is small, this decay takes a nontrivial duration to effectively dissipate.

The corresponding isostable equation is straightforward to derive using the chain rule [49, 45], similar to how we derived (2):

$$\begin{aligned} \frac{d\psi}{dt} &= \nabla\psi \cdot \frac{dX}{dt} \\ &= \nabla\psi \cdot (F(X) + \varepsilon U(X, t)) \\ &= \kappa\psi + \varepsilon I(\theta) \cdot U(X, t), \end{aligned} \quad (6)$$

where the first term follows from (5) and the second term is a simple relabeling of $\nabla\psi$ evaluated on the limit cycle, $I(\theta) \equiv \nabla\psi|_{\Gamma}(\theta)$.

Equation (6) is a useful coordinate to track solutions that decay slowly back to the underlying limit cycle Γ . The order ε term quantifies how incoming perturbations alter the exponential decay of the amplitude. Equation (6) is the second component of the phase-isostable reduction to be used in this paper.

2.3 Phase-Isostable Reduction

We continue following the description in [49, 45, 34] to outline the phase-isostable reduction that will be utilized extensively throughout this paper. We assume that all non-zero Floquet exponents except κ_1 have a large real component (in this case, all other isostable coordinates decay rapidly and are well approximated by zero). For notational convenience, we will simply use ψ and κ to denote the sole non-trivial isostable coordinate and its Floquet exponent.

With this isostable coordinate in hand, we now consider (2) and (6),

$$\begin{aligned} \dot{\theta} &= 1 + \varepsilon \mathcal{Z}(\theta, \psi) \cdot U(X, t), \\ \dot{\psi} &= \kappa\psi + \varepsilon \mathcal{I}(\theta, \psi) \cdot U(X, t) \end{aligned} \quad (7)$$

where the gradient of the phase \mathcal{Z} and the gradient of the isostable \mathcal{I} are each evaluated on the state $X(\theta, \psi)$, which is not necessarily on the periodic orbit (note that $X(\theta, 0) = \Gamma(\theta)$).

The only unknown terms remaining are \mathcal{Z} and \mathcal{I} . These functions are computed using a Taylor expansion centered at $\psi = 0$:

$$\dot{\theta} = 1 + \varepsilon(Z^{(0)}(\theta) + \psi Z^{(1)}(\theta) + \psi^2 Z^{(2)}(\theta) + \dots) \cdot U(X, t), \quad (8)$$

$$\dot{\psi} = \kappa\psi + \varepsilon(I^{(0)}(\theta) + \psi I^{(1)}(\theta) + \psi^2 I^{(2)}(\theta) + \dots) \cdot U(X, t), \quad (9)$$

²Note that it is possible for multiple isostables to decay relatively slowly, in which case we would need to compute additional isostable terms in addition to ψ_1 . More information about how to handle such cases can be found in [49, 46].

where $Z^{(j)}$ and $I^{(j)}$ correspond to the j^{th} order terms in the expansions (note that neglecting the isostable coordinate and the higher-order terms $Z^{(1)}, Z^{(2)}, \dots$ yields the same phase dynamics as the standard phase reduction (2)). These higher-order expansion terms are straightforward to compute [45], and allow the phase-isostable reduction to accurately predict the existence and stability of phase-locked states well beyond the weak coupling regime [48, 33, 34, 28]. From this point forward, any time we mention \mathcal{Z}, \mathcal{I} or their Taylor expansion terms $Z^{(j)}$ and $I^{(j)}$, we assume that they have already been computed numerically.

3 Derivation

We seek phase-locked solutions of the coupled system

$$\begin{aligned} \frac{1}{\omega_X} \frac{dX}{dt} &= F_X(X) + \delta J_X(X) + \varepsilon G_X(X, Y), \\ \frac{1}{\omega_Y} \frac{dY}{dt} &= F_Y(Y) + \delta J_Y(Y) + \varepsilon G_Y(X, Y), \end{aligned} \quad (10)$$

where $F_i : \mathbb{R}^{n_i} \rightarrow \mathbb{R}^{n_i}$ is a smooth vector field, $J_i : \mathbb{R}^{n_i} \rightarrow \mathbb{R}^{n_i}$ is a smooth function describing some additive heterogeneity, $G_i : \mathbb{R}^{n_i} \times \mathbb{R}^{n_j} \rightarrow \mathbb{R}^{n_i}$ is a smooth coupling function, and $n_i \in \mathbb{N}$ for each oscillator $i = X, Y$. The scalar ε (not necessarily small) modulates the overall coupling strength of the network, and the scalar $\delta = O(\varepsilon)$ controls the magnitude of heterogeneity. We also assume,

- Each system in isolation admits a 2π -periodic limit cycle solution (without loss of generality), $\Gamma_i(t_0 + 2\pi) = \Gamma_i(t_0)$, for $i = X, Y$ and some arbitrary time shift $t_0 \in \mathbb{R}$.
- For $\varepsilon = 0$, the system (10) admits a pair of T_X - and T_Y -periodic solutions,

$$X_0(t) = \Gamma_X(\omega_X t), \quad Y_0(t) = \Gamma_Y(\omega_Y t),$$

where

$$nT_X = mT_Y, \quad \omega_X/\omega_Y = n/m, \quad T_X = 2\pi/\omega_X, \quad T_Y = 2\pi/\omega_Y.$$

That is, for every n oscillations traversed by oscillator X_0 , m oscillations are traversed by oscillator Y_0 .

- Limit cycles persist for $\varepsilon \neq 0$ and $\delta \neq 0$ in the coupled system (10).
- All Floquet eigenmodes decay rapidly except in one direction. We denote this nontrivial Floquet exponent by κ_X (κ_Y) for oscillator X (Y). It is straightforward to extend our calculations to the case of multiple nontrivial Floquet exponents so long as they are unique.

Remark 1. *While the assumption that both limit cycles have periods of exactly the ratio $n:m$ at $\varepsilon = \delta = 0$ may seem restrictive, this requirement is equivalent to asserting that it is possible to adjust the period of each system to have exactly such a ratio by adjusting parameters in each model (in neural models, a convenient parameter is the input current). Thus, the ratio $n:m$ does not necessarily imply a loss of generality.*

Remark 2. *We use one parameter for the strength of heterogeneity to simplify calculations, but the proposed method may be extended to any number $M_i \in \mathbb{N}$ of heterogeneous parameters for each oscillator i , e.g., δ_{ij} for $j = 1, \dots, M_i$, with possible nonlinear dependencies on δ_{ij} . Nonlinearities may be handled by truncating Taylor expansions in δ_{ij} . An example of such a formulation for $N \geq 2$ oscillators is discussed in [34].*

Remark 3. Our goal is to verify that the proposed scalar reduction is valid for non-weak (i.e., non-linear) coupling strengths ε in the case of $n:m$ phase-locking. As such, we will typically take expansions up to order $O(\varepsilon^2)$. Higher-order scalar reductions in the coupling strength ε for 1:1 phase-locking may be found in [33, 34].

3.1 Phase-Isostable Reduction

To reduce the system into a set of lower-dimensional equations, we transform (10) into phase coordinates using the chain rule [45], similar to how we applied the chain rule in (2):

$$\begin{aligned}\frac{d\theta_X}{dt} &= \omega_X \nabla \Theta_X \cdot [F_X(X) + \delta J_X(X) + \varepsilon G_X(X, Y)] \\ &= \omega_X [\nabla \Theta_X \cdot F_X(X) + \delta \nabla \Theta_X \cdot J_X(X) + \varepsilon \nabla \Theta_X \cdot G_X(X, Y)] \\ &= \omega_X [1 + \delta \mathcal{Z}_X(X) \cdot J_X(X) + \varepsilon \mathcal{Z}_X(X) \cdot G_X(X, Y)],\end{aligned}\tag{11}$$

where \mathcal{Z}_i is the general phase response function valid for stronger perturbations of the limit cycle beyond the linear regime [45]. Note that the solution X (Y) may be expressed purely in terms of phases θ_X (θ_Y) and isostables ψ_X (ψ_Y), but we keep (11) in terms of X and Y for notational compactness.

The remaining phase-isostable equations for (10) may also be obtained using the chain rule [45, 33, 34], similar to how we applied the chain rule in (2):

$$\begin{aligned}\frac{1}{\omega_X} \frac{d\theta_X}{dt} &= 1 + \mathcal{Z}_X(X) \cdot [\delta J_X(X) + \varepsilon G_X(X, Y)], \\ \frac{1}{\omega_X} \frac{d\psi_X}{dt} &= \kappa_X \psi_X + \mathcal{I}_X(X) \cdot [\delta J_X(X) + \varepsilon G_X(X, Y)], \\ \frac{1}{\omega_Y} \frac{d\theta_Y}{dt} &= 1 + \mathcal{Z}_Y(Y) \cdot [\delta J_Y(Y) + \varepsilon G_Y(X, Y)], \\ \frac{1}{\omega_Y} \frac{d\psi_Y}{dt} &= \kappa_Y \psi_Y + \mathcal{I}_Y(Y) \cdot [\delta J_Y(Y) + \varepsilon G_Y(X, Y)].\end{aligned}\tag{12}$$

To simplify calculations (and following in the same spirit as [7]), we let $s = \omega_Y t$, transforming (12) to,

$$\begin{aligned}\frac{1}{\omega} \theta'_X &= 1 + \varepsilon \mathcal{Z}_X(X) \cdot \hat{G}_X(X, Y), \\ \frac{1}{\omega} \psi'_X &= \kappa_X \psi_X + \varepsilon \mathcal{I}_X(X) \cdot \hat{G}_X(X, Y), \\ \theta'_Y &= 1 + \varepsilon \mathcal{Z}_Y(Y) \cdot \hat{G}_Y(X, Y), \\ \psi'_Y &= \kappa_Y \psi_Y + \varepsilon \mathcal{I}_Y(Y) \cdot \hat{G}_Y(X, Y),\end{aligned}\tag{13}$$

where $' = d/ds$, $\omega := \omega_X/\omega_Y$, $\hat{G}_X(X, Y) = b J_X(X) + G_X(X, Y)$, $\hat{G}_Y(X, Y) = b J_Y(Y) + G_Y(X, Y)$, and $b = \delta/\varepsilon$ (because δ is at most order $O(\varepsilon)$, b is at most order $O(1)$). Note that we treat \hat{G}_i , the sum of G_i and heterogeneity, as a coupling function to simplify the notation when performing the calculations to follow. However, we will be careful to treat J_i and G_i as distinct functions in the results, because even small values of δ can significantly alter phase-locking dynamics.

We begin by expanding all terms in ψ and plugging them into (13), similar to [33, 34, 28]. However, note the key contribution of this paper, where we consider the

case of $n:m$ phase-locking of heterogeneous oscillators as opposed to 1:1 phase-locking of identical oscillators as in previous studies [33, 34, 28]. The expansions are given by,

$$\mathcal{Z}_i(\theta, \psi) \approx Z_i^{(0)}(\theta) + \psi Z_i^{(1)}(\theta) + \psi^2 Z_i^{(2)}(\theta) + \dots, \quad (14)$$

$$\mathcal{I}_i(\theta, \psi) \approx I_i^{(0)}(\theta) + \psi I_i^{(1)}(\theta) + \psi^2 I_i^{(2)}(\theta) + \dots, \quad (15)$$

$$X(t) \approx X_0(\theta_X) + \psi_X g_X^{(1)}(\theta_X) + \psi_X^2 g_X^{(2)}(\theta_X) + \dots, \quad (16)$$

$$Y(t) \approx Y_0(\theta_Y) + \psi_Y g_Y^{(1)}(\theta_Y) + \psi_Y^2 g_Y^{(2)}(\theta_Y) + \dots, \quad (17)$$

where $i = X, Y$, and the functions $Z_i^{(k)}$, $I_i^{(k)}$, and $g_i^{(k)}$ are the higher-order correction terms to the infinitesimal phase response curve ($Z_i^{(0)}$), infinitesimal isostable response curve ($I_i^{(0)}$), and Floquet eigenfunction ($g_i^{(1)}$), respectively (as noted, these correction terms may be computed using straightforward numerical methods [45, 35], and we will assume that these calculations have been done).

We now subtract the moving frame using $\hat{\theta}_X = \theta_X - \omega s$ and $\hat{\theta}_Y = \theta_Y - s$ and plug in the above expansions (14)–(17) into (13), arriving at a set of non-autonomous phase-isostable equations:

$$\begin{aligned} \frac{1}{\omega} \hat{\theta}'_X &= \varepsilon \mathcal{Z}_X(\hat{\theta}_X + \omega s, \psi_X) \cdot \hat{G}_X(\hat{\theta}_X + \omega s, \hat{\theta}_Y + s, \psi_X, \psi_Y), \\ \frac{1}{\omega} \psi'_X &= \kappa_X \psi_X + \varepsilon \mathcal{I}_X(\hat{\theta}_X + \omega s, \psi_X) \cdot \hat{G}_X(\hat{\theta}_X + \omega s, \hat{\theta}_Y + s, \psi_X, \psi_Y), \\ \hat{\theta}'_Y &= \varepsilon \mathcal{Z}_Y(\hat{\theta}_Y + s, \psi_Y) \cdot \hat{G}_Y(\hat{\theta}_X + \omega s, \hat{\theta}_Y + s, \psi_X, \psi_Y), \\ \psi'_Y &= \kappa_Y \psi_Y + \varepsilon \mathcal{I}_Y(\hat{\theta}_Y + s, \psi_Y) \cdot \hat{G}_Y(\hat{\theta}_X + \omega s, \hat{\theta}_Y + s, \psi_X, \psi_Y), \end{aligned} \quad (18)$$

Assumption 1. *We assume that the moving-frame subtracted phase variables, $\hat{\theta}_i$, evolve on a relatively slow timescale compared to the time variable s .*

As our results will show, higher-order averaging is not necessary for the reduced equations to capture nonlinear effects in the coupling strength ε . Heuristically, this property holds because phase differences tend to evolve on significantly slower timescales than the underlying spiking dynamics, even when coupling strengths are well beyond the non-weak regime. The mathematical question of when phase differences tend to maintain this separation of timescales for non-weak coupling will be a topic of future work. In cases where such a timescale separation does not hold, one may utilize higher-order averaging methods from, e.g., [18, 19], which are compatible with the proposed method.

Assumption 1 will aid in applying averaging at a later step, after we've altered the form of the ψ_i equations in (18) so that they are directly amenable to averaging.

3.2 Elimination of Isostable Coordinates

We solve the isostable coordinates to further reduce (18) from 4 dimensions to 2 dimensions (See Discussion 5 for caveats of this approach – in general, this additional dimension reduction may add one-time computational costs at the benefit of an easier phase-locking analysis). To this end, we will perform the following steps:

1. Convert all expansions in ψ_i to expansions in ε using the ansatz

$$\psi_i(s) \approx \varepsilon p_i^{(1)}(s) + \varepsilon^2 p_i^{(2)}(s) + \varepsilon^3 p_i^{(3)}(s) + \dots \quad (19)$$

2. Obtain inhomogeneous linear equations for $p_i^{(k)}$ in a hierarchy of equations in powers of ε .
3. Solve for each $p_i^{(k)}$ to the desired order in ε (this step is handled by a symbolic solver).
4. Plug in each equation for $p_i^{(k)}$ into the phase equation, thus effectively eliminating the isostable variable (note, however, that the isostable dynamics are retained, and perturbed trajectories need not be near the unperturbed limit cycle).

Step 1: Convert all expansions in ψ_i to expansions in ε We plug in the expansion (19) into all terms containing ψ in (18), and collect terms in powers of ε . We then obtain the ε -expansion for terms in \hat{G}_i , such as the heterogeneity functions J_i :

$$J_i(\theta_X, \psi_X) \approx J_i^{(0)}(\theta_X) + \varepsilon J_i^{(1)}(\theta_X, p_X^{(1)}) + \varepsilon^2 J_i^{(2)}(\theta_X, p_X^{(1)}, p_X^{(2)}) + \dots,$$

and the ε -expansion of G_X

$$\begin{aligned} G_X(\theta_X, \theta_Y, \psi_X, \psi_Y) = & K_X^{(0)}(\theta_X, \theta_Y) + \varepsilon K_X^{(1)}\left(\theta_X, \theta_Y, p_X^{(1)}, p_Y^{(1)}\right) \\ & + \varepsilon^2 K_X^{(2)}\left(\theta_X, \theta_Y, p_X^{(1)}, p_X^{(2)}, p_Y^{(1)}, p_Y^{(2)}\right) \\ & + \dots, \end{aligned} \quad (20)$$

where each $K_X^{(\ell)}$ is computed in a manner similar to $J_i^{(\ell)}$. The ε -expansion of G_Y is virtually identical in form to (20) with parity in the indices. Details of how these terms are computed and collected are discussed in Appendix B. In brief, we use a symbolic package to handle the collection of the Taylor expansion of G_X and G_Y , due to the excessive number of terms for even small orders of ε .

The ε -expansions of \mathcal{Z}_i and \mathcal{I}_i are straightforward to obtain by plugging in the ε -expansion of ψ_i (19) into the ψ -expansion of \mathcal{Z}_i (14) and \mathcal{I}_i (14), then collecting in powers of ε using a symbolic package. We then have all terms \mathcal{Z}_i , \mathcal{I}_i , and \hat{G}_i expanded in ε , and can proceed to rewrite the phase-isostable equations (18) in terms of ε . In turn, we obtain a hierarchy of ODEs in powers of ε .

Step 2: Obtain inhomogeneous linear equations for $p_i^{(k)}$ in a hierarchy of equations in powers of ε The left-hand side consists of straightforward time derivatives:

$$\begin{aligned} \frac{1}{\omega} \frac{d}{ds} \psi_X &= \frac{\varepsilon}{\omega} \frac{d}{ds} p_X^{(1)} + \frac{\varepsilon^2}{\omega} \frac{d}{ds} p_X^{(2)} + \frac{\varepsilon^3}{\omega} \frac{d}{ds} p_X^{(3)} + \dots, \\ \frac{d}{ds} \psi_Y &= \varepsilon \frac{d}{ds} p_Y^{(1)} + \varepsilon^2 \frac{d}{ds} p_Y^{(2)} + \varepsilon^3 \frac{d}{ds} p_Y^{(3)} + \dots. \end{aligned}$$

For the right-hand side of ψ_X we have,

$$\begin{aligned}
& \kappa_X \psi_X + \varepsilon \mathcal{I}_X(\hat{\theta}_X + \omega s, \psi_X) \cdot \hat{G}_X(\hat{\theta}_X + \omega s, \hat{\theta}_Y + s, \psi_X, \psi_Y) \\
&= \kappa_X \left(\varepsilon p_X^{(1)} + \varepsilon^2 p_X^{(2)} + \varepsilon^3 p_X^{(3)} + \dots \right) \\
&\quad + \left[\varepsilon \left\{ I_X^{(0)} \right\} + \varepsilon^2 \left\{ p_X^{(1)} I_X^{(1)} \right\} + \varepsilon^3 \left\{ p_X^{(2)} I_X^{(1)} + (p_X^{(1)})^2 I_X^{(2)} \right\} + \dots \right] \\
&\quad \cdot \left[\left\{ bJ_X^{(0)} + K_X^{(0)} \right\} + \varepsilon \left\{ bJ_X^{(1)} + K_X^{(1)} \right\} + \varepsilon^2 \left\{ bJ_X^{(2)} + K_X^{(2)} \right\} + \dots \right] \\
&= \varepsilon \left\{ \kappa_X p_X^{(1)} + I_X^{(0)} \cdot [bJ_X^{(0)} + K_X^{(0)}] \right\} \\
&\quad + \varepsilon^2 \left\{ \kappa_X p_X^{(2)} + I_X^{(0)} \cdot [bJ_X^{(1)} + K_X^{(1)}] + p_X^{(1)} I_X^{(1)} \cdot [bJ_X^{(0)} + K_X^{(0)}] \right\} \\
&\quad + \varepsilon^3 \left\{ \kappa_X p_X^{(3)} + I_X^{(0)} \cdot [bJ_X^{(2)} + K_X^{(2)}] + p_X^{(1)} I_X^{(1)} \cdot [bJ_X^{(1)} + K_X^{(1)}] \right. \\
&\quad \left. + [p_X^{(2)} I_X^{(1)} + (p_X^{(1)})^2 I_X^{(2)}] \cdot [bJ_X^{(0)} + K_X^{(0)}] \right\},
\end{aligned}$$

where we have suppressed the following function dependencies to keep the notation less cluttered: $p_i^{(\ell)}(s)$, $I_X^{(\ell)}(\hat{\theta}_X + \omega s)$, $J_X^{(0)}(\hat{\theta}_X + \omega s)$, $J_X^{(1)}(\hat{\theta}_X + \omega s, p_X^{(1)})$, $J_X^{(2)}(\hat{\theta}_X + \omega s, p_X^{(1)}, p_X^{(2)})$, $K_X^{(0)}(\hat{\theta}_X + \omega s, \hat{\theta}_Y + s)$, $K_X^{(1)}(\hat{\theta}_X + \omega s, \hat{\theta}_Y + s, p_X^{(1)}, p_Y^{(1)})$, and $K_X^{(2)}(\hat{\theta}_X + \omega s, \hat{\theta}_Y + s, p_X^{(1)}, p_X^{(2)}, p_Y^{(1)}, p_Y^{(2)})$. The right-hand side of ψ_Y follows similarly.

Consolidating terms for each order in ε yields the following hierarchy of ODEs (starting with order $O(\varepsilon)$),

$$\begin{aligned}
\frac{1}{\omega} \frac{dp_X^{(1)}}{ds} &= \kappa_X p_X^{(1)} + I_X^{(0)} \cdot [bJ_X^{(0)} + K_X^{(0)}], \\
\frac{1}{\omega} \frac{dp_X^{(2)}}{ds} &= \kappa_X p_X^{(2)} + I_X^{(0)} \cdot [bJ_X^{(1)} + K_X^{(1)}] + p_X^{(1)} I_X^{(1)} \cdot [bJ_X^{(0)} + K_X^{(0)}], \\
\frac{1}{\omega} \frac{dp_X^{(3)}}{ds} &= \kappa_X p_X^{(3)} + I_X^{(0)} \cdot [bJ_X^{(2)} + K_X^{(2)}] + p_X^{(1)} I_X^{(1)} \cdot [bJ_X^{(1)} + K_X^{(1)}] \\
&\quad + [p_X^{(2)} I_X^{(1)} + (p_X^{(1)})^2 I_X^{(2)}] \cdot [bJ_X^{(0)} + K_X^{(0)}], \\
&\quad \vdots
\end{aligned} \tag{21}$$

The hierarchy of ODEs for $p_Y^{(\ell)}$ follows similarly. Here, we notice that all ODEs are first-order inhomogeneous differential equations with forcing terms that depend on lower-order solutions. As such, we can solve each ODE explicitly and pre-compute them.

Step 3: Solve for each $p_i^{(k)}$ to the desired order in ε It is straightforward to solve (21) with a combination of symbolic and numerical methods, but we show some explicit calculations for concreteness. We begin with the lowest-order term, rewritten here with explicit dependencies for convenience:

$$\frac{1}{\omega} \frac{dp_X^{(1)}}{ds} = \kappa_X p_X^{(1)}(s) + I_X^{(0)}(\hat{\theta}_X + \omega s) \cdot [bJ_X^{(0)}(\hat{\theta}_X + \omega s) + K_X^{(0)}(\hat{\theta}_X + \omega s, \hat{\theta}_Y + s)]$$

The solution may be found using standard methods from an introductory undergraduate differential equations course:

$$\begin{aligned} p_X^{(1)}(s) &= \omega \int_0^s e^{\omega \kappa_X (s-r)} I_X^{(0)}(\hat{\theta}_X + \omega r) \cdot K_X^{(0)}(\hat{\theta}_X + \omega r, \hat{\theta}_Y + r) dr \\ &\quad + \omega b \int_0^s e^{\omega \kappa_X (s-r)} I_X^{(0)}(\hat{\theta}_X + \omega r) \cdot J_X^{(0)}(\hat{\theta}_X + \omega r) dr \\ &\quad + p_X^{(1)}(0) e^{\omega \kappa_X s}. \end{aligned}$$

Assumption 2. For each fixed $\hat{\theta}_X, \hat{\theta}_Y$, each $p_i^{(\ell)}$ term has transients that may be safely ignored.

This assumption allows us to rewrite the domain of integration from $[0, s]$ to $(-\infty, s]$ and drop the initial condition:

$$\begin{aligned} p_X^{(1)}(s) &= \omega \int_{-\infty}^s e^{\omega \kappa_X (s-r)} I_X^{(0)}(\hat{\theta}_X + \omega r) \cdot K_X^{(0)}(\hat{\theta}_X + \omega r, \hat{\theta}_Y + r) dr \\ &\quad + \omega b \int_{-\infty}^s e^{\omega \kappa_X (s-r)} I_X^{(0)}(\hat{\theta}_X + \omega r) \cdot J_X^{(0)}(\hat{\theta}_X + \omega r) dr. \end{aligned}$$

With the change of variables $r' = s - r$, the above equation becomes

$$\begin{aligned} p_X^{(1)}(s) &= \omega \int_0^\infty e^{\omega \kappa_X r} I_X^{(0)}(\hat{\theta}_X + \omega(s-r)) \cdot \hat{K}_X^{(0)}(\hat{\theta}_X + \omega(s-r), \hat{\theta}_Y + s-r) dr \\ &\quad + \omega b \int_0^\infty e^{\omega \kappa_X r} I_X^{(0)}(\hat{\theta}_X + \omega(s-r)) \cdot J_X^{(0)}(\hat{\theta}_X + \omega(s-r)) dr. \end{aligned}$$

For convenience and by definition, this function may be viewed purely as a function of the original fast phase variables θ_X, θ_Y :

$$\begin{aligned} p_X^{(1)}(\theta_X, \theta_Y) &= \omega \int_0^\infty e^{\omega \kappa_X r} I_X^{(0)}(\theta_X - \omega r) \cdot \hat{K}_X^{(0)}(\theta_X - r\omega, \theta_Y - r) dr \\ &\quad + \omega b \int_0^\infty e^{\omega \kappa_X r} I_X^{(0)}(\theta_X - \omega r) \cdot J_X^{(0)}(\theta_X - r\omega) dr. \end{aligned}$$

By an identical argument,

$$\begin{aligned} p_Y^{(1)}(\theta_X, \theta_Y) &= \int_0^\infty e^{\kappa_Y r} I_Y^{(0)}(\theta_Y - r) \cdot K_Y^{(0)}(\theta_X - r\omega, \theta_Y - r) dr \\ &\quad + b \int_0^\infty e^{\kappa_Y r} I_Y^{(0)}(\theta_Y - r) \cdot J_Y^{(0)}(\theta_Y - r) dr. \end{aligned}$$

Because $p_X^{(1)}$ and $p_Y^{(1)}$ only depend on phase variables, these functions may be pre-computed numerically. The numerical computation can be made especially efficient by rewriting the above as a 1D convolution (see Appendix D). Note that while $p_Y^{(1)}(\theta_X, \theta_Y)$ is written in terms of fast phase variables, precomputing this quantity does not violate any separation of timescales. The dependence of $p_Y^{(1)}$ on (θ_X, θ_Y) is simply a shorthand – what we have really computed is $p_Y^{(1)}(s) \equiv p_Y^{(1)}(\hat{\theta}_X + \omega s, \hat{\theta}_Y + s)$. That is, we've explicitly solved for $p_X^{(1)}$ in terms of s as desired, given the relatively constant phase variables $\hat{\theta}_X$ and $\hat{\theta}_Y$. Because $p_X^{(1)}$ is periodic in each coordinate³, we only need to compute $p_X^{(1)}(s)$ for one period in s for each pair of slow variables $(\hat{\theta}_X, \hat{\theta}_Y) \in [0, 2\pi] \times [0, 2\pi]$.

³Periodicity of $p_X^{(1)}(s)$ follows from periodicity of its forcing functions, e.g., $I_X^{(0)}(\hat{\theta}_X + \omega(s + 2\pi - r)) = I_X^{(0)}(\hat{\theta}_X + \omega(s - r))$.

We next solve $p_X^{(2)}$ ($p_Y^{(2)}$) for order $k = 2$. The forcing function for $p_X^{(2)}$ ($p_Y^{(2)}$) includes the term $p_X^{(1)}(\theta_X, \theta_Y)$ ($p_Y^{(1)}(\theta_X, \theta_Y)$), or equivalently, $p_X^{(1)}(\hat{\theta}_X + \omega s, \theta_Y + s)$ ($p_Y^{(1)}(\hat{\theta}_X + \omega s, \theta_Y + s)$). These functions are integrated in the fast variable s in the same manner as above to solve for $p_X^{(2)}(\theta_X, \theta_Y)$ ($p_Y^{(2)}(\theta_X, \theta_Y)$).

We may continue this process to include as many higher-order terms $p_X^{(\ell)}(\theta_X, \theta_Y)$, $p_Y^{(\ell)}(\theta_X, \theta_Y)$ as needed, thus obtaining explicit terms for the coefficients of the ψ_i ε -expansion $\psi_X = \varepsilon p_X^{(1)} + \varepsilon^2 p_X^{(2)} + \dots$ ($\psi_Y = \varepsilon p_Y^{(1)} + \varepsilon^2 p_Y^{(2)} + \dots$), effectively eliminating the ψ_X (ψ_Y) equations (without requiring that solutions remain near the unperturbed limit cycle).

Remark 4. *The heterogeneity parameter b appears in each solution $p_X^{(\ell)}$ (or $p_Y^{(\ell)}$) up to the power b^ℓ .*

The intuition behind this remark is straightforward to confirm by taking $J_X = (1, 0, \dots, 0)^\top$, and $J_Y = 0$ so that the heterogeneity parameter b only appears in the first coordinate of oscillator X . Then, $\hat{K}_X^{(0)} = K_X^{(0)} + (b, 0, \dots, 0)^\top$ and $\hat{K}_X^{(\ell)} = K_X^{(\ell)}$ for $\ell \geq 1$. With this choice of heterogeneity, the solution of $p_X^{(1)}$ will have an additive term scaled by b . It then follows that the right-hand side of $p_X^{(2)}$, which contains the term $p_X^{(1)} I_X^{(1)} \cdot (K_X^{(0)} + (b, 0, \dots, 0)^\top)$, will contain a b^2 term. It is possible to argue inductively to higher powers. We rely on automated symbolic manipulation to handle these calculations for us, but we refer the reader to the derivation in [34] for additional details in the case of 1:1 phase-locking with $N \geq 2$ oscillators.

Now that we have solved for each $p_i^{(\ell)}$, we turn to writing down an explicit phase difference equation.

Step 4: Plug in the ε -expansions of ψ_i into the phase equations, thus effectively eliminating the isostable variable To provide a bird's-eye view, we perform the average,

$$\begin{aligned} \frac{1}{\omega} \hat{\theta}'_X &= \frac{1}{2\pi m} \int_0^{2\pi m} \mathcal{Z}_X(\hat{\theta}_X + \omega s, \hat{\theta}_Y + s) \cdot \hat{G}_X(\hat{\theta}_X + \omega s, \hat{\theta}_Y + s) ds, \\ \hat{\theta}'_Y &= \frac{1}{2\pi m} \int_0^{2\pi m} \mathcal{Z}_Y(\hat{\theta}_X + \omega s, \hat{\theta}_Y + s) \cdot \hat{G}_Y(\hat{\theta}_X + \omega s, \hat{\theta}_Y + s) ds, \end{aligned}$$

where we momentarily abuse notation and let $\hat{\theta}_i$ denote the averaged version of the variables $\hat{\theta}_i$ and do not explicitly include the ψ_i or $p_i^{(\ell)}$ terms because they are included implicitly. By applying the transformation $s \rightarrow \theta_Y + s$, we arrive at a more convenient form,

$$\begin{aligned} \frac{1}{\omega} \hat{\theta}'_X &= \frac{1}{2\pi m} \int_0^{2\pi m} \mathcal{Z}_X(\hat{\theta}_X - \omega \hat{\theta}_Y + \omega s, s) \cdot \hat{G}_X(\hat{\theta}_X - \omega \hat{\theta}_Y + \omega s, s) ds, \\ \hat{\theta}'_Y &= \frac{1}{2\pi m} \int_0^{2\pi m} \mathcal{Z}_Y(\hat{\theta}_X - \omega \hat{\theta}_Y + \omega s, s) \cdot \hat{G}_Y(\hat{\theta}_X - \omega \hat{\theta}_Y + \omega s, s) ds. \end{aligned}$$

These equations are useful because the integrals can be expressed as functions of the phase difference $\phi = \hat{\theta}_X - \omega \hat{\theta}_Y$, which will further reduce the dimension of the system into a scalar equation. For the following calculations, we resume working explicitly with $bJ_X(X) + G_X(X, Y)$ ($bJ_Y(Y) + G_Y(X, Y)$) as opposed to $\hat{G}_X(X, Y)$ ($\hat{G}_Y(X, Y)$).

Substituting the expansion for ψ_X and collecting in powers of ε yields a virtually identical right-hand side as (21) with Z in place of I :

$$\begin{aligned}
\frac{1}{\omega} \hat{\theta}'_X &= \varepsilon Z_X^{(0)} \cdot K_X^{(0)} + \varepsilon^2 \left(Z_X^{(0)} \cdot K_X^{(1)} + p_X^{(1)} Z_X^{(1)} \cdot K_X^{(0)} \right) \\
&\quad + \varepsilon^3 \left(Z_X^{(0)} \cdot K_X^{(2)} + p_X^{(1)} Z_X^{(1)} \cdot K_X^{(1)} + p_X^{(2)} Z_X^{(1)} \cdot K_X^{(0)} + \left(p_X^{(1)} \right)^2 Z_X^{(2)} \cdot K_X^{(0)} \right) \\
&\quad + \dots \\
&\quad + \varepsilon b Z_X^{(0)} \cdot J_X^{(0)} + \varepsilon^2 b \left(Z_X^{(1)} J_X^{(0)} + Z_X^{(0)} J_X^{(1)} \right) \\
&\quad + \varepsilon^3 b \left(Z_X^{(2)} J_X^{(0)} + Z_X^{(1)} J_X^{(1)} + Z_X^{(0)} J_X^{(2)} \right) \\
&\quad + \dots,
\end{aligned} \tag{22}$$

Similarly,

$$\begin{aligned}
\hat{\theta}'_Y &= \varepsilon Z_Y^{(0)} \cdot K_Y^{(0)} + \varepsilon^2 \left(Z_Y^{(0)} \cdot K_Y^{(1)} + p_Y^{(1)} Z_Y^{(1)} \cdot K_Y^{(0)} \right) \\
&\quad + \varepsilon^3 \left(Z_Y^{(0)} \cdot K_Y^{(2)} + p_Y^{(1)} Z_Y^{(1)} \cdot K_Y^{(1)} + p_Y^{(2)} Z_Y^{(1)} \cdot K_Y^{(0)} + \left(p_Y^{(1)} \right)^2 Z_Y^{(2)} \cdot K_Y^{(0)} \right) \\
&\quad + \dots \\
&\quad + \varepsilon b Z_Y^{(0)} \cdot J_Y^{(0)} + \varepsilon^2 b \left(Z_Y^{(1)} J_Y^{(0)} + Z_Y^{(0)} J_Y^{(1)} \right) \\
&\quad + \varepsilon^3 b \left(Z_Y^{(2)} J_Y^{(0)} + Z_Y^{(1)} J_Y^{(1)} + Z_Y^{(0)} J_Y^{(2)} \right) \\
&\quad + \dots.
\end{aligned} \tag{23}$$

Note that the heterogeneity parameter b is implicitly taken to higher orders as argued in Remark 4.

We average each $O(\varepsilon^\ell)$ term in (22) and (23), yielding a system of autonomous phase equations

$$\frac{1}{\omega} \theta'_X = b \sum_{\ell=1}^M \varepsilon^\ell \mathcal{J}_X^{(\ell)} + \sum_{\ell=1}^M \varepsilon^\ell \left[\mathcal{H}_X^{(\ell)}(\theta_X - \omega \theta_Y) \right], \tag{24}$$

$$\theta'_Y = b \sum_{\ell=1}^M \varepsilon^\ell \mathcal{J}_Y^{(\ell)} + \sum_{\ell=1}^M \varepsilon^\ell \left[\mathcal{H}_Y^{(\ell)}(\theta_X - \omega \theta_Y) \right], \tag{25}$$

where

$$\begin{aligned}
\mathcal{J}_i^{(1)} &= \frac{1}{2\pi} \int_0^{2\pi} Z_i^{(0)}(s) \cdot J_i^{(0)}(s) \, ds, \\
\mathcal{J}_i^{(2)} &= \frac{1}{2\pi} \int_0^{2\pi} Z_i^{(1)}(s) \cdot J_i^{(0)}(s) + Z_i^{(0)}(s) \cdot J_i^{(1)}(s) \, ds, \\
\mathcal{J}_i^{(3)} &= \frac{1}{2\pi} \int_0^{2\pi} Z_i^{(2)}(s) \cdot J_i^{(0)}(s) + Z_i^{(1)}(s) \cdot J_i^{(1)}(s) + Z_i^{(0)}(s) \cdot J_i^{(2)}(s) \, ds, \\
&\vdots
\end{aligned}$$

and

$$\begin{aligned}
\mathcal{H}_X^{(1)}(\xi) &= \frac{1}{2\pi m} \int_0^{2\pi m} Z_X^{(0)}(\xi + \omega s) \cdot K_X^{(0)}(\xi + \omega s, s) \, ds, \\
\mathcal{H}_X^{(2)}(\xi) &= \frac{1}{2\pi m} \int_0^{2\pi m} Z_X^{(0)}(\xi + \omega s) \cdot K_X^{(1)}(\xi + \omega s, s) \\
&\quad + p_X^{(1)}(\xi + \omega s, s) Z_X^{(1)}(\xi + \omega s) \cdot K_X^{(0)}(\xi + \omega s, s) \, ds, \\
\mathcal{H}_X^{(3)}(\xi) &= \frac{1}{2\pi m} \int_0^{2\pi m} Z_X^{(0)}(\xi + \omega s) \cdot K_X^{(2)}(\xi + \omega s, s) \\
&\quad + p_X^{(1)}(\xi + \omega s, s) Z_X^{(1)}(\xi + \omega s) \cdot K_X^{(1)}(\xi + \omega s, s) \\
&\quad + p_X^{(2)}(\xi + \omega s, s) Z_X^{(1)}(\xi + \omega s) \cdot K_X^{(0)}(\xi + \omega s, s) \\
&\quad + p_X^{(1)}(\xi + \omega s, s)^2 Z_X^{(2)}(\xi + \omega s) \cdot K_X^{(0)}(\xi + \omega s, s) \, ds, \\
&\vdots
\end{aligned}$$

Again, the heterogeneity parameter b is implicit.

Similarly,

$$\begin{aligned}
\mathcal{H}_Y^{(1)}(\xi) &= \frac{1}{2\pi m} \int_0^{2\pi m} Z_Y^{(0)}(\xi + \omega s) \cdot K_Y^{(0)}(\xi + \omega s, s) \, ds, \\
\mathcal{H}_Y^{(2)}(\xi) &= \frac{1}{2\pi m} \int_0^{2\pi m} Z_Y^{(0)}(\xi + \omega s) \cdot K_Y^{(1)}(\xi + \omega s, s) \\
&\quad + p_Y^{(1)}(\xi + \omega s, s) Z_Y^{(1)}(\xi + \omega s) \cdot K_Y^{(0)}(\xi + \omega s, s) \, ds, \\
\mathcal{H}_Y^{(3)}(\xi) &= \frac{1}{2\pi m} \int_0^{2\pi m} Z_Y^{(0)}(\xi + \omega s) \cdot K_Y^{(2)}(\xi + \omega s, s) \\
&\quad + p_Y^{(1)}(\xi + \omega s, s) Z_Y^{(1)}(\xi + \omega s) \cdot K_Y^{(1)}(\xi + \omega s, s) \\
&\quad + p_Y^{(2)}(\xi + \omega s, s) Z_Y^{(1)}(\xi + \omega s) \cdot K_Y^{(0)}(\xi + \omega s, s) \\
&\quad + p_Y^{(1)}(\xi + \omega s, s)^2 Z_Y^{(2)}(\xi + \omega s) \cdot K_Y^{(0)}(\xi + \omega s, s) \, ds, \\
&\vdots
\end{aligned}$$

Defining $\phi = \theta_X - \omega \theta_Y$, the corresponding ordinary differential equation is given by

$$\begin{aligned}
\phi' &= \theta'_X - \omega \theta'_Y \\
&= \omega \sum_{\ell=1}^M \varepsilon^\ell \left(\mathcal{J}_X^{(\ell)} - \mathcal{J}_Y^{(\ell)} \right) b + \omega \sum_{\ell=1}^M \varepsilon^\ell \left(\mathcal{H}_X^{(\ell)}(\phi) - \mathcal{H}_Y^{(\ell)}(\phi) \right).
\end{aligned}$$

Finally, defining $\mathcal{H}_{n,m}^{(\ell)}(\phi) = \mathcal{H}_X^{(\ell)}(\phi) - \mathcal{H}_Y^{(\ell)}(\phi)$, and $b^{(\ell)} = (\mathcal{J}_X^{(\ell)} - \mathcal{J}_Y^{(\ell)})b$, the phase difference dynamics is given by the scalar equation,

$$\frac{1}{\omega} \phi' = \sum_{\ell=1}^M \varepsilon^\ell [b^{(\ell)} + \mathcal{H}_{n,m}^{(\ell)}(\phi)]. \quad (26)$$

Remarks:

- In the coupling case, there is an implicit dependence on the heterogeneity term b inside the functions $b^{(\ell)}$ and $\mathcal{H}_{n,m}^{(\ell)}(\phi)$ in Equation (26), because for nonzero b ,

each forcing function of $p_i^{(\ell)}$ will also contain b (up to the power b^ℓ). We show an example of the phase reduction with explicit heterogeneity b up to order $O(\varepsilon^2)$ in Appendix E, which is used to calculate two-parameter bifurcation diagrams in Section 4.2.

- In the forcing case, changes to the forcing frequency simply results in a vertical shift of the $\mathcal{H}_{n,m}^{(\ell)}$ functions because the dependence on the heterogeneity parameter δ is completely described by $b^{(\ell)}$ in (26) (see Section 4.1).

4 Results

We first examine how well the scalar reduction captures phase-locking in a forced non-radial isochron clock (Section 4.1.1) and a forced thalamic neuron (Section 4.1.2). We then test the scalar reduction for a coupled pair of thalamic neurons with heterogeneity for multiple combinations of $n:m$ phase-locking (Section 4.2.1).

4.1 Forcing

We use the same formulation (26) to reduce a forced oscillator into a scalar variable, which represents the phase difference between the exogenous forcing function and the phase of the forced oscillator. In particular, let ω_Y be the forcing frequency and $G_X(X, \omega_Y t)$ be the “coupling” function. Then our original coupled system (10) becomes

$$\begin{aligned} \frac{1}{\omega_X} \frac{dX}{dt} &= F_X(X) + \varepsilon G_X(X, \theta_Y), \\ \frac{1}{\omega_Y} \frac{d\theta_Y}{dt} &= 1 + \delta/\omega_Y, \end{aligned} \tag{27}$$

where the heterogeneity parameter δ directly modulates the forcing frequency. The choice to include the heterogeneity term directly in the right-hand side of $d\theta_Y/dt$ is without loss of generality for the following reason. If we take Y in (10) to be some oscillator that forces oscillator X (so $G_Y \equiv 0$), then δ alters the vector fields of each oscillator, generically resulting in a change to their natural frequencies. This relative difference in frequencies can simply be captured by directly modifying the natural frequency of the forcing oscillator ω_Y .

The corresponding scalar reduction for (27) is given by

$$\frac{1}{\omega} \phi' = -\frac{\delta}{\omega_Y} + \sum_{\ell=1}^M \varepsilon^\ell \mathcal{H}_{n,m}^{(\ell)}(\phi), \tag{28}$$

where we have implicitly used the same assumptions from the coupling case that there is a reasonable separation of timescales between $\hat{\theta}_X$ ($\hat{\theta}_Y$) and s . Note that higher powers of b do not appear in the forcing case, and δ remains an order $O(\varepsilon)$ parameter. Thus, linear changes to the forcing frequency only yield linear shifts to the \mathcal{H} functions.

There are no particular restrictions on the choice of forcing function besides sufficient smoothness and periodicity. While choosing a sinusoidal function such as $\cos(\omega_Y t)$ would be a good starting point, the lack of nontrivial Fourier modes simplifies the existence of phase-locking to 1:1 as in the case of the nonradial isochron clock, or to $n:1$ as in the case of the forced thalamic model. Thus, we use a periodized Gaussian to ensure that there are enough nontrivial Fourier modes to explore $n:m$ phase-locking for $n, m \geq 1$.

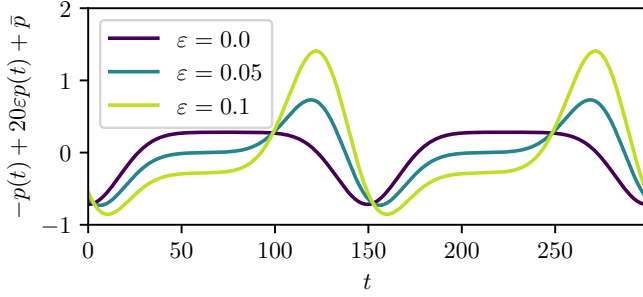


Figure 1: The forcing function (29) as a function of ε . The large second-order term results in a significant deformation of the forcing function as ε increases from $\varepsilon = 0$ to $\varepsilon = 0.1$.

We define the periodized forcing function as

$$p(\omega_Y t) = \sum_{i=-\infty}^{\infty} \exp\left(-(\omega_Y(t + 2\pi i)/\sigma)^2\right).$$

We numerically implement this function by truncating the infinite sum (e.g., only considering indices i such that $|i| \leq 3$) and taking the input modulo 2π . Importantly, we also include a second-order term in ε as part of the forcing function. This choice reflects the assumption that strong perturbations in nature do not necessarily scale linearly. Thus, the forcing function used throughout this section is given by,

$$G(X, \omega_Y t) \equiv G(\omega_Y t) = -p(\omega_Y t) + 20\varepsilon p(\omega_Y(t + 1)) + \bar{p}, \quad (29)$$

where \bar{p} is the mean of p on $[0, 2\pi/\omega_Y]$. The large second-order term is chosen so that the forcing function exhibits a large deformation in its second-order term. This choice will help us verify the accuracy of the non-linear terms in the scalar reduction. A plot of the forcing function is shown in Figure 1 for various values of ε .

4.1.1 Nonradial Isochron Clock

The nonradial isochron clock [48, 34] is defined as

$$\begin{aligned} \frac{1}{\omega_X} \frac{dX}{dt} &= F_{\text{NR}}(X) + \varepsilon[G(\theta_Y), 0]^\top, \\ \frac{1}{\omega_Y} \frac{d\theta_Y}{dt} &= 1 + \delta/\omega_Y, \end{aligned} \quad (30)$$

where $X = [x, y]^\top$,

$$F_{\text{NR}}(X) = \begin{pmatrix} \sigma x(1 - R^2) - y(1 + \rho(R^2 - 1)) \\ \sigma y(1 - R^2) + x(1 + \rho(R^2 - 1)) \end{pmatrix},$$

$R = \sqrt{x^2 + y^2}$, $\sigma = 0.08$, and $\rho = 0.12$. The Floquet exponent of the isolated limit cycle (at $\varepsilon = 0$) is $\kappa_X \approx -0.16$, making it weakly attracting enough to suitably test the proposed method.

Remark 5. *We are limited to testing n:1 phase-locking for the nonradial isochron clock because the Fourier modes of the model's response functions typically only contain the*

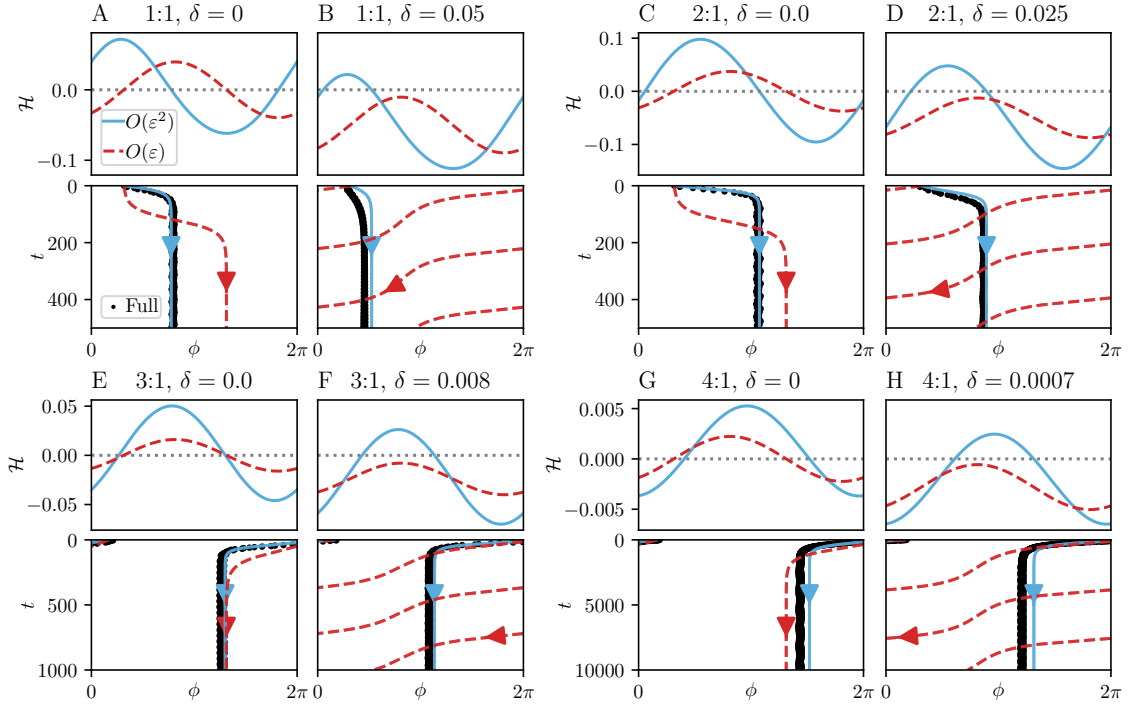


Figure 2: Frequency-locking and drift in a forced nonradial isochron clock. All panels use the same horizontal axis, $\phi \in [0, 2\pi]$. Each label (A–H) corresponds to particular values of ε and δ , and each labeled panel has two sub-panels, top and bottom. Each top panel shows the right-hand sides of the first order (dashed red) and second order (solid blue) scalar reductions. The zeros of these functions (where they intersect the dashed gray line) correspond to phase-locked states in the full model. Each bottom panel shows the solutions of the first (dashed red) and second-order scalar reductions (solid blue) and full model (black) over time. A, B: 1:1 phase-locking for $\delta = 0, 0.05$ respectively, with initial condition $\phi(0) = 1$. C, D: 2:1 phase-locking for $\delta = 0, 0.025$, respectively, with $\phi(0) = 1$. E, F: 3:1 phase-locking for $\delta = 0, 0.008$, respectively, with $\phi(0) = 0.5$. G, H: 4:1 phase-locking for $\delta = 0, 0.0007$, respectively, with $\phi(0) = 0.5$. We plot every two-hundredth point in the full model's phase estimate to reduce lag when viewing the figure. $\varepsilon = 0.1$ in all panels except G, H, where $\varepsilon = 0.06$.

principal harmonic. This feature poses a minor problem: for example, if we choose a forcing function with half a period compared to the original oscillator ($\omega_Y = 2$ and $\omega_X = 1$), then the integrals involved in computing the \mathcal{H} -functions cancel due to orthogonality, and there is no phase-locking. A similar issue arises when choosing a pure sinusoid for the forcing function, such as $\cos(\omega_Y t)$. The \mathcal{H} -functions will only be nontrivial when $\omega_X = \omega_Y$, i.e., only 1:1 phase-locking can exist.

Trajectories of the full and reduced nonradial isochron clock are shown in Figure 2. Phase differences in the full model are estimated using the limit cycle computed at $\varepsilon = 0$ (see Appendix C for more details). Each panel (A–H) corresponds to particular values of ε and δ , plotted with solutions of the scalar reduction (dashed red for $O(\varepsilon)$ and solid blue for $O(\varepsilon^2)$) and the full model (black). We choose the coupling strength to be $\varepsilon = 0.1$ ($\varepsilon = 0.06$ for Panels G, H) to test how well the higher-order scalar reduction captures $n:1$ coupling. Across all panels, the second-order reduction is consistently able to better predict the existence of phase-locked states in the presence of heterogeneity (when $\delta > 0$).

While the second-order reduction captures phase-locked states more accurately relative to the first-order reduction, our goal is also to predict where the original system

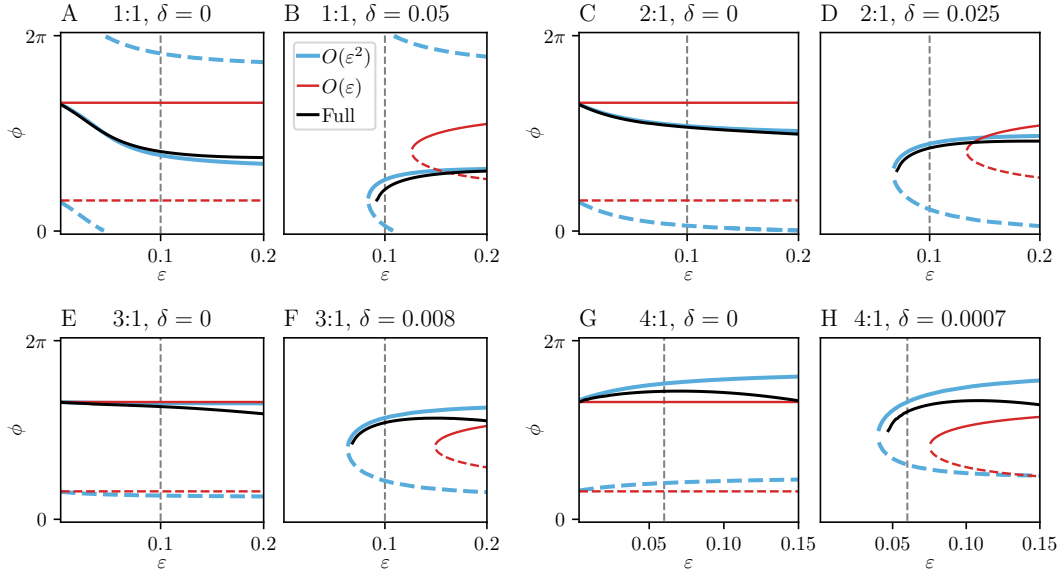


Figure 3: One-parameter bifurcation diagrams of the forced nonradial isochron clock as a function of coupling strength ε . The order $O(\varepsilon)$ scalar reduction is shown in red, the order $O(\varepsilon^2)$ scalar reduction is shown in blue, and the stable phase-locked states of the original system is shown in black. Each panel A–H corresponds to the same system in panels A–H of Figure 2. Solid (dashed) curves denote stable (unstable) fixed points of the scalar reduction. The vertical gray dashed lines correspond to the ε parameter value used in the corresponding panel in Figure 2.

loses the existence of phase-locked states due to nonzero heterogeneity δ and non-weak forcing strength ε . To better quantify how and when the second-order reduction loses phase-locked states (and compare these predictions to the original model), we compute one-parameter bifurcation diagrams in ε given varying degrees of heterogeneity δ , along with two-parameter bifurcation diagrams in ε and δ .

One-parameter bifurcation diagrams of reduced and full nonradial isochron clock are shown in Figure 3. The diagrams were computed numerically by tracking fixed points in the reduced model, and by computing phase-locked states using Newton’s method in the full model. We simply assume the period of the phase-locked solution to be given directly by the forcing frequency. If Newton’s method converges to a periodic solution, then there exists a phase-locked solution. This convergence typically happens in under 10 iterations, assuming that the correction vector has a tolerance of 1×10^{-6} . However, if Newton’s method fails to converge in 20 iterations, we assume that there is no phase-locked solution.

Note that we are unable to use XPPAUTO to generate one or two-parameter bifurcation diagrams due to the choice of forcing function. If the forcing function is sinusoidal, then the standard approach is to augment the system with a pair of *autonomous* ODEs that have sinusoidal functions as solutions (see [8] Section 7.4). In contrast, our choice of forcing function involves Gaussians – while Gaussians do have a corresponding ODE, the ODE happens to be non-autonomous. For this reason, attempting to compute bifurcation diagrams will fail in XPPAUTO.

All panels A–H of this figure correspond to the same underlying model in panels A–H in Figure 2. The second-order scalar reduction is significantly more capable of capturing the existence of frequency-locked states as a function of ε for representative values of δ compared to the first-order reduction. Note that the values of δ at which frequency-locking is lost differ by orders of magnitude between 1:1 locking (Figure 2A,B or Figure

3A,B) and 4:1 locking (Figure 2G,H or Figure 3G,H). This observation is consistent with the fact that Fourier coefficients become vanishingly small as $n \rightarrow \infty$ in $n:1$ locking, and that the bandwidth of $n:m$ locking decreases as a function of higher frequencies [7].

Two-parameter bifurcation diagrams of the reduced nonradial isochron clock are shown in Figure 4. The diagrams were computed numerically using XPPAUT [8] using Fourier approximations of the \mathcal{H} -functions in the scalar reduction up to $O(\varepsilon^2)$. Coefficients of the Fourier approximation of each \mathcal{H} -function may be found in Appendix E. The phase-locking regions in Figure 4 are equivalent to Arnold tongues, except that each horizontal axis shows the heterogeneity parameter δ as opposed to the more standard frequency ratio.

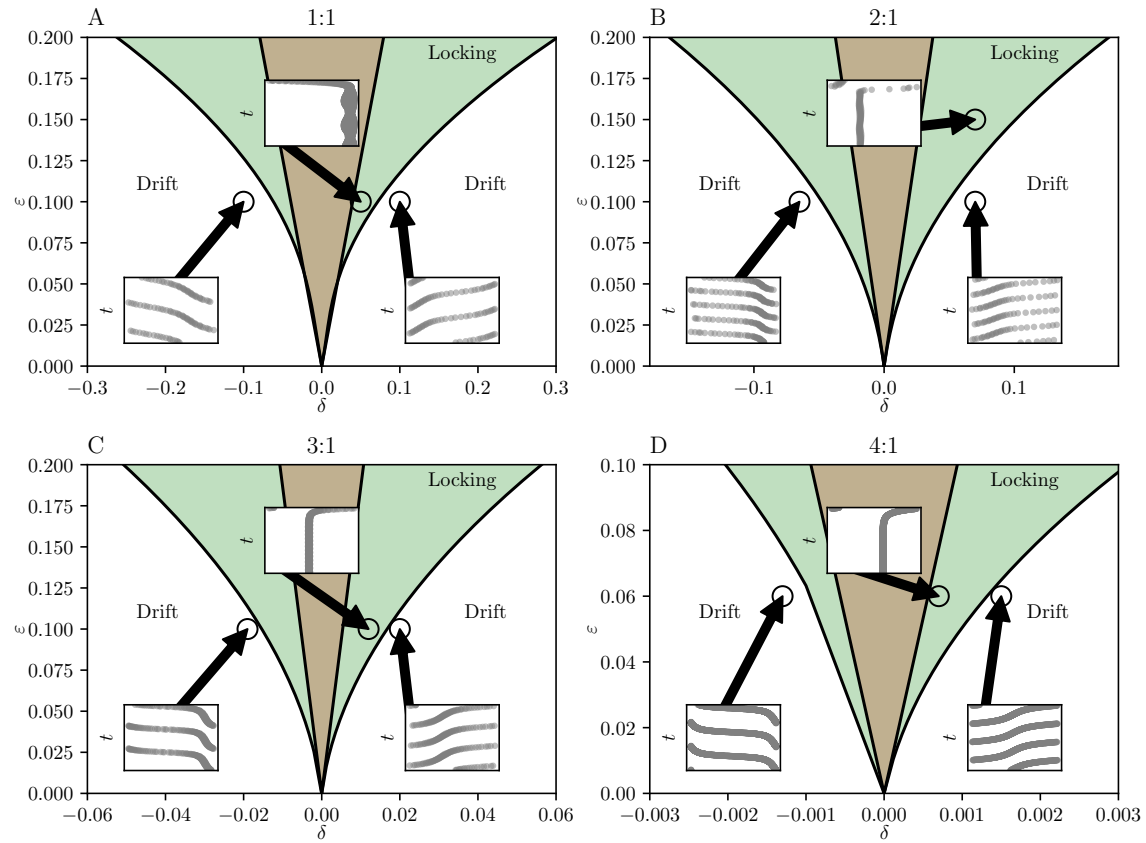


Figure 4: Two-parameter bifurcation diagrams (Arnold tongues) of the forced nonradial isochron clock. The vertical axis is the forcing amplitude ε , and the horizontal axis is the forcing frequency change δ . Green (red) shaded regions correspond to stable phase-locking regions prediction by the $O(\varepsilon^2)$ ($O(\varepsilon)$) scalar reduction. Insets show the full model dynamics over time for representative choices of δ and ε . ε and δ Parameter choices are as follows, from left to right for each panel. A: $(\delta, \varepsilon) = (-0.1, 0.1), (0.05, 0.1), (0.1, 0.1)$. B: $(\delta, \varepsilon) = (-0.065, 0.1), (0.07, 0.15), (0.07, 0.1)$. C: $(\delta, \varepsilon) = (-0.019, 0.1), (0.012, 0.1), (0.02, 0.12)$. D: $(\delta, \varepsilon) = (-0.0013, 0.06), (0.0007, 0.06), (0.0015, 0.06)$.

Table 1: Parameter values of the nondimensionalized thalamic model (31)

Parameter	E_K	E_{Na}	E_t	E_L	g_L	g_K	g_{Na}	$g_{syn} \equiv \varepsilon$	I_{app}	α	β
Value	-0.9	0.5	0	-0.7	0.05	5	3	0-0.3	0.035	3	2

4.1.2 Thalamic Neuron

We now consider a nondimensionalized model of a thalamic neuron⁴ (adapted from [37]),

$$\begin{aligned} \frac{1}{\omega_X} \frac{dX}{dt} &= F_{Thal}(X) + \varepsilon[G(\theta_Y), 0, 0]^\top, \\ \frac{1}{\omega_Y} \frac{d\theta_Y}{dt} &= 1 + \delta/\omega_Y, \end{aligned} \quad (31)$$

where $X = [V, h, r]^\top$,

$$F_{Thal}(X) = \begin{pmatrix} -I_L(V) - I_{Na}(V) - I_K(V) - I_T(V) + I_{app} \\ (h_\infty(V) - h)/\tau_h(V) \\ (r_\infty(V) - r)/\tau_r(V) \end{pmatrix}.$$

We use the same forcing function as used in the nonradial isochron example, rewritten here for convenience:

$$G(\theta_Y) \equiv G(\omega_Y t) = -p(\omega_Y t) + 20\varepsilon p(\omega_Y(t+1)) + \bar{p},$$

where p is a periodized Gaussian. Recall that the relatively large second-order term was chosen to test how well the scalar reduction captures non-weak (and therefore non-linear) forcing strengths. The remaining equations are given by

$$\begin{aligned} I_L(V) &= g_L(V - E_L), & I_{Na}(V) &= g_{Na} h m_\infty^3(V)(V - E_{Na}), \\ I_K(V) &= g_K[0.75(1 - h)]^4(V - E_K), & I_T(V) &= g_T r p_\infty^2(V)(V - E_T), \end{aligned}$$

and

$$\begin{aligned} a_h(V) &= 0.128 \exp(-5.556(V + 0.46)), & b_h(V) &= 4/(1 + \exp(-20(V + 0.23))), \\ m_\infty(V) &= 1/(1 + \exp(-14.29(V + 0.37))), & h_\infty(V) &= 1/(1 + \exp(25(V + 0.41))), \\ r_\infty(V) &= 100/(1 + \exp(25(V + 0.84))), & p_\infty(V) &= 0.01/(1 + \exp(-16.13(V + 0.6))), \\ \tau_h(V) &= 1/(a_h(V) + b_h(V)), & \tau_r(V) &= 28 + \exp(-9.52(V + 0.25)), \\ a_\infty(V) &= 1/(1 + \exp(-125(V + 0.2))). \end{aligned}$$

Nondimensional parameter values are listed in Table 1. The Floquet exponent of the isolated limit cycle (at $\varepsilon = 0$) is $\kappa_X \approx -0.024$, making it weakly attracting enough to suitably test the proposed method.

The first and second-order scalar reductions are compared to the full model in Figure 5. We now consider a different set of frequency ratios because $n:m$ locking is now possible for $n, m > 1$. In particular, we choose 1:1, 2:1, 1:2, and 2:3 for the purpose of illustration. In panels where $\delta > 0$ (Figure 5B, D, F, H), the second-order reduction is consistently

⁴To obtain the original thalamic model from [37], multiply the voltage by 100 mV, and divide the gating variable r by 100 mV. Conductances are scaled using 1 nS. We choose the characteristic scale of 100 mV because it is similar in magnitude to the potassium reversal potential ($E_K = -90$ mV).

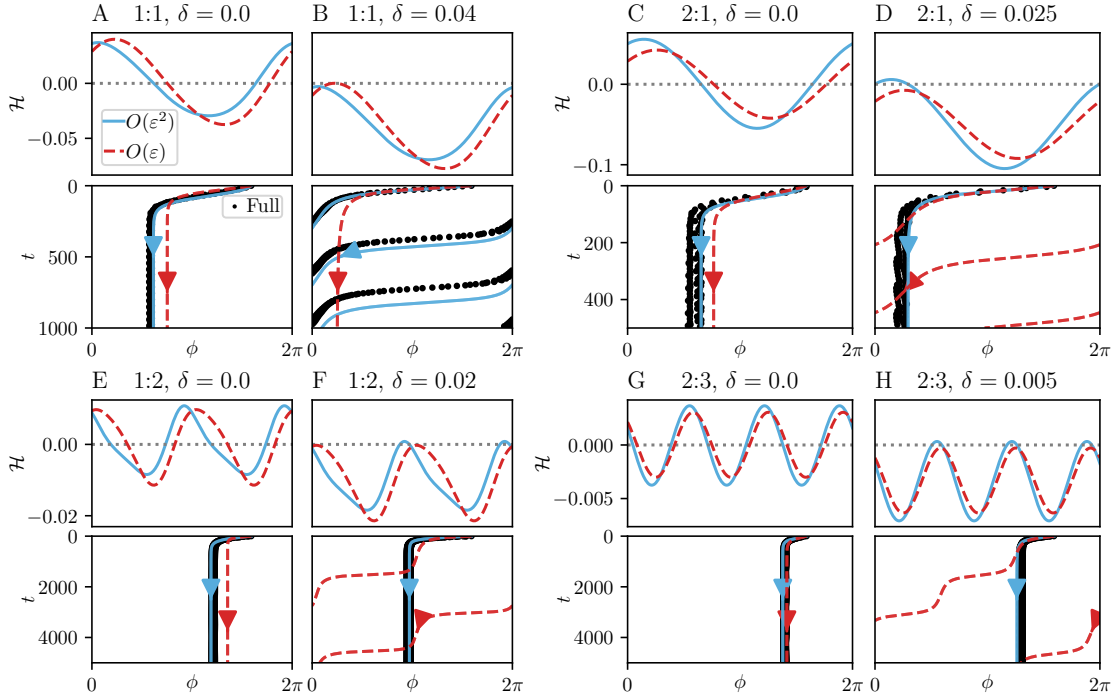


Figure 5: Frequency-locking and drift in a forced thalamic neuron. All panels use the same horizontal axis, $\phi \in [0, 2\pi]$. Each label (A–H) corresponds to particular values of ε and δ , and each labeled panel has two sub-panels, top and bottom. Each top panel shows the right-hand sides of the first order (dashed red) and second order (solid blue) scalar reductions. The zeros of these functions (where they intersect the dashed gray line) correspond to phase-locked states in the full model. Each bottom panel shows the solutions of the first (dashed red) and second-order scalar reductions (solid blue) and full model (black) over time. All panels use the initial condition $\phi(0) = 5$. A, B: 1:1 phase-locking for $\delta = 0, 0.04$ respectively, and $\varepsilon = 0.023$. C, D: 2:1 phase-locking for $\delta = 0, 0.025$, respectively, and $\varepsilon = 0.025$. E, F: 1:2 phase-locking for $\delta = 0, 0.02$, respectively, and $\varepsilon = 0.035$. G, H: 2:3 phase-locking for $\delta = 0, 0.005$, respectively, and $\varepsilon = 0.022$. We plot every two-hundredth point in the full model's phase estimate to reduce lag when viewing the figure.

better able to capture the existence (or non-existence) of phase-locked states relative to the first-order reduction. Phase differences in the full model are estimated using the limit cycle computed at $\varepsilon = 0$ (see Appendix C for more details).

Just as in the previous example of the nonradial isochron clock, our goal is also to predict where the original system loses the existence of phase-locked states due to nonzero heterogeneity δ and non-weak forcing strength ε , and thus compute one-parameter bifurcation diagrams in ε given varying degrees of heterogeneity δ , along with two-parameter bifurcation diagrams in ε and δ .

One-parameter bifurcation diagrams of reduced and full thalamic neuron are shown in Figure 6. The diagrams were computed numerically by tracking fixed points in the reduced model, and by computing phase-locked states using Newton's method in the full model. Note that we are unable to use XPPAUT to generate one or two-parameter bifurcation diagrams due to the choice of forcing function, as stated in Section 4.1.1. All panels A–H of Figure 6 correspond to the same underlying model in panels A–H in Figure 5. The second-order scalar reduction is significantly more capable of capturing the existence of frequency-locked states as a function of ε for representative values of δ compared to the first-order reduction.

Two-parameter bifurcation diagrams of the reduced thalamic neuron are shown in

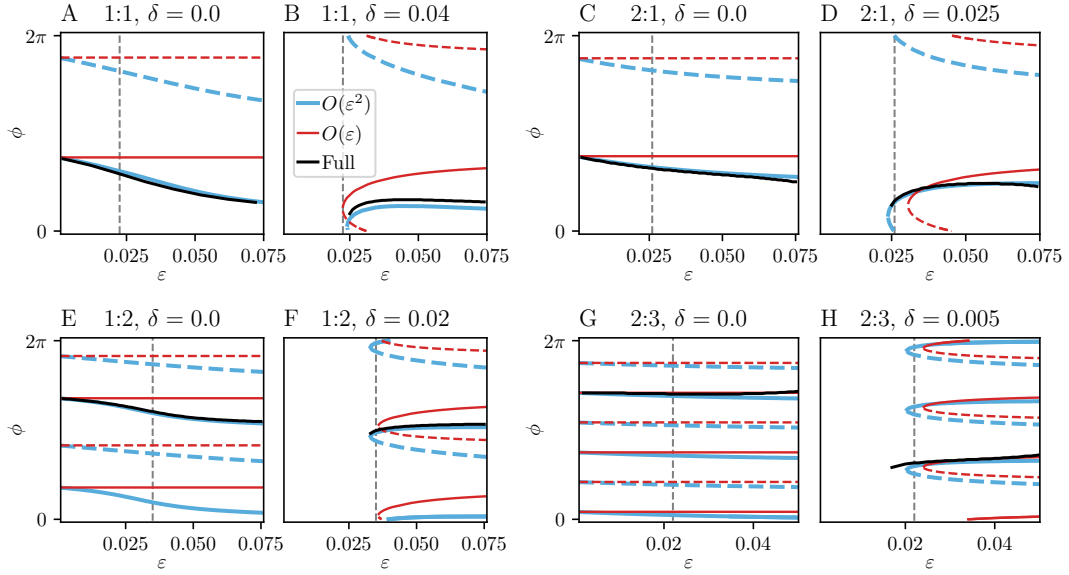


Figure 6: One-parameter bifurcation diagrams of a forced thalamic neuron as a function of coupling strength ε . The order $O(\varepsilon)$ scalar reduction is shown in red, the order $O(\varepsilon^2)$ scalar reduction is shown in blue, and the stable phase-locked states of the original system are shown in black. Each panel A–H corresponds to the same system in panels A–H of Figure 5. Solid (dashed) curves denote stable (unstable) fixed points of the scalar reduction. The vertical gray dashed lines correspond to the ε parameter value used in the corresponding panel in Figure 5. We show only one bifurcation curve of the full model (black), to aid in comparisons with the reduced bifurcations (red and blue). Generating all bifurcation curves for the full model for panels E, F, G, and H, simply resemble phase-shifted copies of itself.

Figure 7. The diagrams were computed numerically using XPPAUTO [8] using Fourier approximations of the \mathcal{H} -functions in the scalar reduction up to $O(\varepsilon^2)$. Coefficients of the Fourier approximation of each \mathcal{H} -function may be found in Appendix E. The phase-locking regions in Figure 7 are equivalent to Arnold tongues, except that each horizontal axis shows the heterogeneity parameter δ as opposed to the more standard frequency ratio.

4.2 Coupling

4.2.1 A Pair of Thalamic Neurons with Heterogeneity

We now consider a pair of synaptically coupled thalamic neurons (adapted from [37]). The model is identical to the forced thalamic model (31) (including the same parameters as in Table 1), but we include an additional variable (w) representing a chemical synapse:

$$\hat{F}_{\text{Thalamic}}(X) = \begin{pmatrix} F_{\text{Thalamic}}(X) \\ \alpha(1-w)a_\infty(V) - \beta w \end{pmatrix},$$

where $X = [V_1, h_1, r_1, w_1]^\top$ ($Y = [V_2, h_2, r_2, w_2]^\top$). The coupled equations are given by,

$$\begin{aligned} \frac{1}{\omega_X} \frac{dX}{dt} &= \hat{F}_{\text{Thalamic}}(X) + \delta_1 + \delta_2^2 + \varepsilon[G_2(X, Y)]^\top, \\ \frac{1}{\omega_Y} \frac{dY}{dt} &= \hat{F}_{\text{Thalamic}}(Y) + \varepsilon[G_2(Y, X)]^\top, \end{aligned} \tag{32}$$

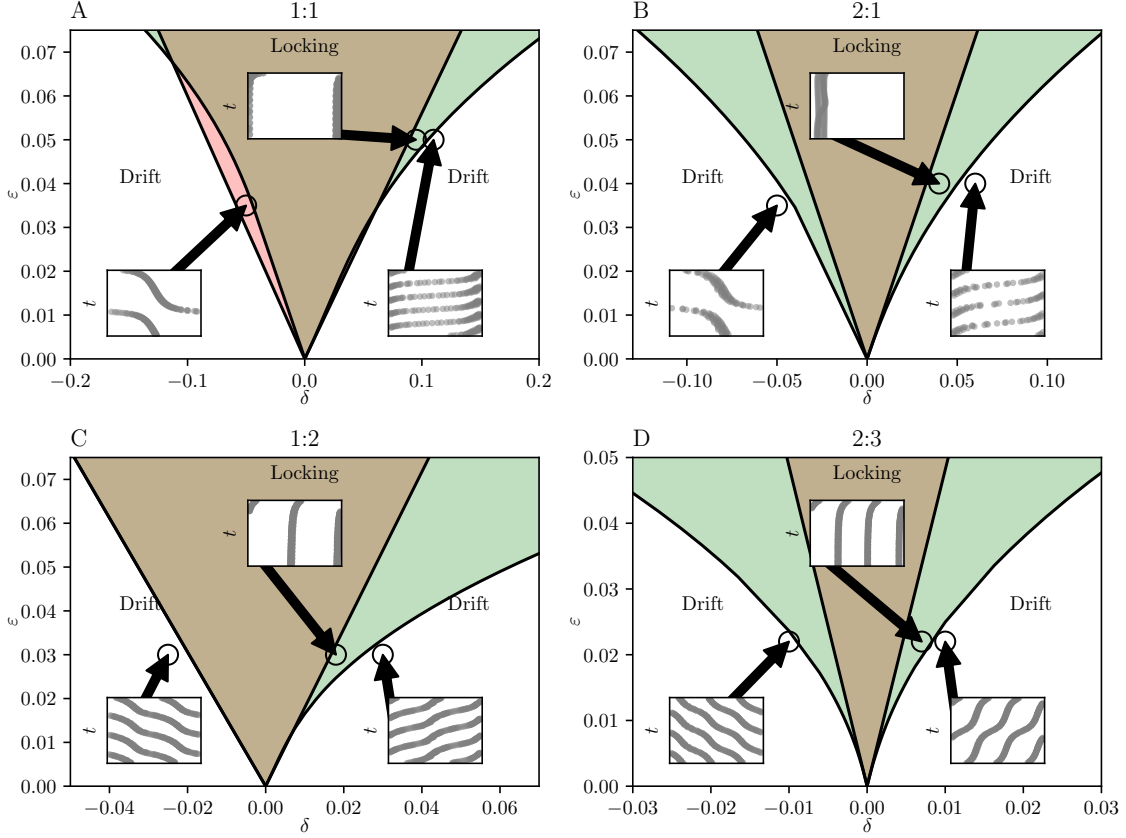


Figure 7: Two-parameter bifurcation diagrams (Arnold tongues) of a forced thalamic neuron. The vertical axis is the forcing amplitude ε , and the horizontal axis is the forcing frequency change δ . Green (red) shaded regions correspond to stable phase-locking regions prediction by the $O(\varepsilon^2)$ ($O(\varepsilon)$) scalar reduction. Insets show the full model dynamics over time for representative choices of δ and ε . ε and δ Parameter choices are as follows, from left to right for each panel. A: $(\delta, \varepsilon) = (-0.05, 0.035), (0.095, 0.05), (0.11, 0.05)$, for 500 time units. B: $(\delta, \varepsilon) = (-0.05, 0.035), (0.04, 0.04), (0.06, 0.04)$, for 250 time units. C: $(\delta, \varepsilon) = (-0.025, 0.03), (0.018, 0.03), (0.03, 0.03)$, for 1000 time units. D: $(\delta, \varepsilon) = (-0.01, 0.022), (0.007, 0.022), (0.01, 0.022)$, for 1000 time units.

where $\varepsilon \equiv g_{\text{syn}}$ is the synaptic conductance, and

$$G_2(X, Y) = [w_2(V_1 - E_{\text{syn}}), 0, 0, 0]^\top.$$

We choose an excitatory synapse with $E_{\text{syn}} = 0$.

The higher-order heterogeneity terms δ_i are assumed to take the forms,

$$\delta_1 \equiv \varepsilon b c_1, \quad \delta_2 \equiv \varepsilon b c_2,$$

where c_1 and c_2 represent arbitrary coefficients of a Taylor expansion, and b is a fixed heterogeneity parameter. In principle, there can be an infinite number of Taylor coefficients c_i , but we are only interested in testing whether the scalar reduction properly captures non-linear effects of heterogeneity. Thus, choosing only c_1 and c_2 is equivalent to truncating a Taylor expansion of the heterogeneity function J .

We choose $c_2 \gg c_1$ because we generally have that $\varepsilon b \ll 1$. For instance, for 3:4 phase-locking, we choose $c_1 = 1$ and $c_2 = 1 \times 10^3$, where c_2 is not as excessively large as it may seem at first glance. First, c_2 is the coefficient for a term that is $\varepsilon^2 b^2 \ll \varepsilon b \ll 1$,

so c_2 must be exaggerated for non-linear effects to be noticeable. Second, for even modestly greater values of n and m , such as $n = 3$ and $m = 4$, only small changes to b lead to noticeable changes in phase-locked states, often on the order of $b = 1 \times 10^{-3}$. Then, b^2 is on the order of 1×10^{-6} , and the second-order coefficient $c_2 b^2$ is on the order of 1×10^{-3} for 3:4 phase-locking, which is reasonable. So the exaggerated choices for c_2 ultimately lead to more natural second-order coefficients.

We remark that the simple choice of the heterogeneity terms also leads to cases where phase-locking may not only be lost by increasing the magnitude of heterogeneity b , but also regained. Consider the heterogeneity terms with $b < 0$:

$$\begin{aligned}\delta_1 + \delta_2^2 &= \varepsilon b c_1 + \varepsilon^2 b^2 c_2 \\ &= -\varepsilon |b| c_1 + \varepsilon^2 |b|^2 c_2.\end{aligned}$$

Suppose, for concreteness, that $c_1 = 1$, $c_2 = 1000$, and $\varepsilon = 0.1$. Then,

$$\delta_1 + \delta_2^2 = -0.1|b| + 10|b|^2.$$

If we set this equation to zero, we find two distinct values of $|b|$ that result in zero total heterogeneity:

$$|b|(-0.1 + 10|b|) = 0,$$

where $|b| = 0$ or $|b| = 0.1$. Since we assumed $b < 0$, the only possible non-trivial root is $b = -0.1$. This observation shows that the resumption of phase-locking with this choice of heterogeneity is due to a cancellation of lower- and higher-order heterogeneity terms (note that the same cancellation above is possible for $b > 0$ if $c_1 = -1$). In actual systems, such a perfect cancellation is unlikely, and we make no claims about whether or not it occurs in nature. It is nevertheless a notable feature of our chosen example, which is captured by the proposed reduction.

The resulting scalar reduction takes the form,

$$\phi' = \varepsilon[\mathcal{H}_{n,m}^{(1)}(\phi) + b] + \varepsilon^2[\mathcal{H}_{n,m}^{(2)}(\phi) + b\mathcal{J}_1]$$

Trajectories of the scalar reduction and full model are shown in Figure 8 for $n:m$ coupling. Phase differences in the full model are estimated using the limit cycle computed at $\varepsilon = 0$ (see Appendix C). The second-order scalar reduction (blue) is better able to reproduce phase-locked states than the first-order scalar reduction (red dashed) for all combinations of phase-locked states and heterogeneity, including 1:1 (Figure 8A), 1:2 (Figure 8B), 2:1 (Figure 8C), 1:3 (Figure 8D), 3:1 (Figure 8E), 2:3 (Figure 8F), 3:2 (Figure 8G), 3:4 (Figure 8H), and 4:3 (Figure 8I).

The one-parameter bifurcation diagram for 1:1 phase-locking is shown in Figure 9. Because the coupling strength term ε always multiplies the heterogeneity term b , the system tends to be much less sensitive to changes in ε for a fixed value of b , as shown in Figure 9 Panels A and B. Intuitively, for our choice of the thalamic model, there happen to be fewer higher-order effects due to coupling strength. In addition, the heterogeneity b and the synaptic coupling terms scale similarly as a function of ε (in large part because we defined the heterogeneity to scale with ε). Thus, changes to coupling strength alone will not reveal significant differences between the first and second-order reductions. In contrast, more interesting changes are visible in Panels C and D, where we fix the coupling strength ε and alter the heterogeneity b . The higher-order effects of heterogeneity are especially visible in Panel D, due to the increased coupling strength ε , which also happens to exaggerate the higher-order effects of heterogeneity.

Note that while we lose phase-locking by decreasing b to be more negative, it is also possible for phase-locking to resume if b is decreased further. For this example, we have $c_1 = 1$ and $c_2 = 100$. Then, assuming $b < 0$ and $\varepsilon = 0.1$,

$$\delta_1 + \delta_2^2 = \varepsilon b c_1 + \varepsilon^2 b^2 c_2 = -0.1|b| + 1|b|^2.$$

The zeros are given by $|b| = 0$ and $|b| = 0.1$, so phase-locking resumes when $b = -0.1$. If we choose ε to be lesser, then b will have to be much greater in magnitude to recover phase-locking (see the two-parameter diagram for 1:1 phase-locking in Figure 12A).

Similar diagrams for the remaining combinations of phase-locking in Figure 8 are shown in Figure 10 (for 1:2, 2:1, 1:3, 3:1), and Figure 11 (for 2:3, 3:2, 3:4, 4:3), with the same corresponding values of c_i as in Figure 8.

Two-parameter bifurcation diagrams of the scalar reduction are shown in Figure 12. We only show the second-order reduction because the lowest-order reduction only has vertical boundaries that separate the stable phase-locking regions from phase drift (i.e., the phase-locking regions are independent of the coupling strength). This observation can be proven simply by considering an equivalent form of our first-order reduction:

$$x' = \varepsilon(h_1(x) + b h_2(x)),$$

where x is a scalar and $h_i : \mathbb{R} \rightarrow \mathbb{R}$. If $x = x^*$ is the coordinate of a saddle-node given $b = b^*$ and $\varepsilon = \varepsilon^*$, then by definition, we also have the following conditions satisfied:

$$\begin{aligned} 0 &= \varepsilon^*(h_1(x^*) + b^* h_2(x^*)), \\ 0 &= \varepsilon^*(h'_1(x^*) + b^* h'_2(x^*)). \end{aligned}$$

Note, then, that so long as x^* and b^* are held constant, the conditions for the saddle-node will be satisfied for any ε^* , thus proving that the first-order scalar reduction will not capture meaningful two-parameter bifurcation diagrams.

These results demonstrate that the proposed phase-reduction is robustly and reliably able to reduce the dimension of realistic conductance-based neural models for $n:m$ phase-locking with heterogeneity.

5 Discussion

We have demonstrated that the proposed scalar reduction captures the same existence (or non-existence) of phase-locked states as the corresponding full model for various values of the coupling strength ε beyond the weak regime, and for nonlinear heterogeneous effects δ_i (or b), for various combinations of $n:m$ phase-locking.

We first highlight some important observations. Across virtually all results, the magnitude of heterogeneity b is often only needs to be orders of magnitude smaller than ε to yield significant changes to the existence and stability of phase-locked states. This observation suggests that methods like H/K theory, that show the existence and stability of fixed points for even very strong coupling, may ultimately find limited use in biologically realistic contexts, where heterogeneity is an important (if not necessary) part of function.

5.1 Limitations

The proposed scalar reduction relies on having a reasonable separation of timescales between the phase difference dynamics and the limit cycle period, so that first-order

averaging can be used to turn non-autonomous equations into relatively tractable autonomous equations. However, the results show that first-order averaging is sufficient to capture nonlinear effects in both heterogeneity and coupling strength.

While the scalar reduction captures saddle-node bifurcations in phase-locked states, it is by nature unable to capture Hopf bifurcations in phase-locked states for a pair of oscillators. The scalar model also cannot capture transient oscillations toward phase-locked states that happen to be stable foci, although it can capture the existence and asymptotic stability of stable foci. Note, however, that for three or more oscillators, the scalar model can capture Hopf bifurcations in the phase difference dynamics as demonstrated in [34].

5.2 Utility of the Proposed Method

Despite potential limitations, the proposed scalar reduction retains significant utility. Multiple authors have already developed and demonstrated scalar reductions well beyond the weak coupling regime using this type of scalar reduction [48, 33, 34, 22], but their results were restricted to 1:1 phase-locking, and typically without heterogeneity. While there are existing works on scalar reductions with heterogeneity such as [22], their results apply only to planar systems, whereas this paper establishes a natural extension to n dimensional systems. We have also made the notation for heterogeneity more concrete and considered a coupling example that is more biologically realistic. Indeed, the proposed formulation for heterogeneity is not just restricted to the case of $N = 2$ oscillators as in [22]. A generalization of this formulation to $N \geq 2$ and n -dimensional oscillators is discussed in [34] for 1:1 phase-locking. The generalization to $n:m$ phase-locking for $N \geq 2$ oscillators will be the topic of future work. Nevertheless, the current results are an important generalization, because we can now more closely analyze oscillators with non-equal periods beyond the weak coupling regime.

There is also practical utility of the proposed formulation: it is extremely efficient to integrate numerically, because the integrator only references an interpolating function for each $\mathcal{H}_i^{(\ell)}$ function. Integrating the scalar reduction often takes orders of magnitude less time to integrate than the full system, while also being much simpler to analyze.

The proposed reduction may be used to introduce more realistic forms of coupling functions to idealized models such as the Kuramoto model. The classic Kuramoto model only uses a pure sine function to describe coupling, but the proposed method may be used to include additional sinusoidal terms that approximate the Fourier expansion of more biologically realistic coupling functions. This idea may be applied naturally beyond the Kuramoto model, e.g., to the higher-order reduction of the Haken-Kelso-Bunz (HKB) equation in [24], which considers the lowest-order Fourier coefficients of the \mathcal{H} -functions of the proposed method. Additional Fourier modes may be computed and added as needed.

A Newton’s Method for Phase-Locking

Let f be the function that maps $g^\alpha(0)$ to $g^\alpha(T)$ for a particular g^α we are looking for. Assuming $g^*(0)$ is a close guess for the periodic solution, $f(g^*(0)) = g^*(T)$. We then

look for a vector Δg that solves for the periodic solution [44], i.e.,

$$\begin{aligned} f(g^*(0) + \Delta g) &= g^*(0) + \Delta g, \\ \Rightarrow f(g^*(0)) + J\Delta g &= g^*(0) + \Delta g, \\ \Rightarrow (J - I)\Delta g &= g^*(0)f(g^*(0)), \\ \Rightarrow \Delta g &= (J - I)^{-1}(g^*(0) - f(g^*(0))), \end{aligned}$$

where J is the Jacobian matrix of f , and I is the identity matrix. The function f is the stroboscopic map after the times $T = nT_X$ or $T = mT_Y$, where the quantities T or T_i are estimated by simulating the coupled system for sufficiently long times until it converges to a phase-locked state.

The Jacobian matrix J is estimated as follows. Take an initial condition, i.e., an initial guess $Y(0)$ on or near the limit cycle. Without loss of generality, consider two spatially-perturbed initial conditions, $Y_1(0) = Y(0) + [\varepsilon, 0, \dots, 0]$ and $Y_2(0) = Y(0) - [\varepsilon, 0, \dots, 0]$. We integrate each initial condition forward in time up to time T , where we obtain the estimate of the first column of the Jacobian matrix, $(Y_2(T) - Y_1(T))/(2\varepsilon)$. Repeat this process for the remaining columns of J .

To include the time estimate T in the Newton iteration, we augment J with a column given by two solutions $Z_1(T + \varepsilon)$ and $Z_2(T - \varepsilon)$ with initial conditions $Z_1(0) = Z_2(0) = Y(0)$. We then augment J with a new row, with the last row and column set to zero, and the remaining elements of the last row given by the right-hand side of the coupled system evaluated on the initial condition $Y(0)$.

When starting the Newton iteration, the term $g^*(0)$ is given by the initial guess $Y(0)$ and $f(g^*(0))$ is given by the time integration of the coupled system given the initial condition $Y(0)$ up to time T . Once Δg is computed, it is used to update the initial guess $Y(0)$ (simply, $Y(0) \rightarrow Y(0) + \Delta g$, which is used as the new initial condition for the next iteration.

For all Newton iterations, we use a perturbation size of $\varepsilon = 1 \times 10^{-4}$. The condition to stop the iteration is determined by the magnitude of $\|Y(0)\|$ – if $\|Y(0)\| \leq 1 \times 10^{-5}$, then we say the system has converged to a phase-locked state. If the number of iterations exceeds 20 without the magnitude reducing below the desired tolerance, we assume that there is no phase-locked solution.

In the case of forcing, we exclude the time condition because there is no stability information from the forcing function. Instead, we only compute the Jacobian given the spatially-perturbed solutions, and take the integration time T to be the period of the forcing function. Then, the condition for convergence are the same as the coupling case.

B Coupling Term Expansions

To expand the coupling functions G_i in powers of ε , we use the Floquet eigenfunction approximation $(g_i^{(k)})$ for each oscillator,

$$\begin{aligned} \Delta X &\approx \psi_X g_X^{(1)}(\theta_X) + \psi_X^2 g_X^{(2)}(\theta_X) + \dots, \\ \Delta Y &\approx \psi_Y g_Y^{(1)}(\theta_Y) + \psi_Y^2 g_Y^{(2)}(\theta_Y) + \dots, \end{aligned} \tag{33}$$

where $\Delta X \equiv X(t) - X_0(\theta_X(t))$ ($\Delta Y \equiv Y(t) - Y_0(\theta_Y(t))$) is the difference between the limit cycle solution X_0 (Y_0) and an arbitrary trajectory $X(t)$ ($Y(t)$) in the basin of attraction. We focus on G_X without loss of generality because the calculations are identical for G_Y , \hat{G}_i , and J_i .

We view the coupling function as the map $G_X : \mathbb{R}^{n_X+n_Y} \rightarrow \mathbb{R}^{n_X}$, where

$$G_X(\Xi) = [G_{X,1}(\Xi), G_{X,2}(\Xi), \dots, G_{X,n_X}(\Xi)]^\top \in \mathbb{R}^{n_X},$$

$$G_{X,m} : \mathbb{R}^{n_X+n_Y} \rightarrow \mathbb{R}, \quad m = 1, 2, \dots, n_X,$$

and $\Xi = [X^\top, Y^\top]^\top \in \mathbb{R}^{n_X+n_Y}$ is an $(n_X + n_Y) \times 1$ column vector. To make the expansion explicit, we write $\Xi = \Lambda + \Delta\Xi$, where

$$\Lambda = [X_0(\theta_X)^\top, Y_0(\theta_Y)^\top]^\top \in \mathbb{R}^{n_X+n_Y},$$

$$\Delta\Xi = [\Delta X^\top, \Delta Y^\top]^\top \in \mathbb{R}^{n_X+n_Y},$$

so both are $(n_X + n_Y) \times 1$ column vectors. We now use the “vec” operator from [20, 45] to obtain the multivariate Taylor expansion of $G_{X,m}$ for each $m = 1, 2, \dots, n_X$:

$$G_{X,m}(\Lambda + \Delta\Xi) = G_{X,m}(\Lambda) + G_{X,m}^{(1)}(\Lambda)\Delta\Xi + \sum_{k=2}^{\infty} \frac{1}{k!} \left[\otimes^k \Delta\Xi^\top \right] \text{vec} \left(G_{X,m}^{(k)}(\Lambda) \right), \quad (34)$$

where \otimes is the Kronecker product, and, temporarily treating Λ as a vector of dummy variables,

$$G_{X,m}^{(k)}(\Lambda) = \frac{\partial \text{vec} \left(G_{X,m}^{(k-1)}(\Lambda) \right)}{\partial \Lambda^\top} \in \mathbb{R}^{(n_X+n_Y)^{(k-1)} \times (n_X+n_Y)}. \quad (35)$$

The vec operator simply reshapes a matrix by stacking its columns, which allows us to avoid calculating high-dimensional tensors. For example, if an $n \times m$ matrix A has columns a_i for $i = 1, \dots, n$ for $a_i \in \mathbb{R}^m$, then $\text{vec}(A)$ is the $mn \times 1$ column vector $(a_1^\top, a_2^\top, \dots, a_n^\top)^\top$. If A is a Jacobian matrix, taking partial derivatives yields a tensor, whereas taking partials of $\text{vec}(A)$ yields a matrix.

B.1 Concrete Calculations

For concreteness, we show explicit expansion terms of $G_{X,m}$ up to order ψ^2 and follow up with the order ε^3 expansion. The lowest-order term $G_{X,m}^{(0)}(\Lambda)$ is trivial, so we examine the next-order term, $G_{X,m}^{(1)}(\Lambda)\Delta\Xi$. We first compute the first derivative using the vec notation,

$$G_{X,m}^{(1)}(\Lambda) = \frac{\partial \text{vec} \left(G_{X,m}^{(0)}(\Lambda) \right)}{\partial \Lambda^\top}$$

$$\equiv \left(\partial_{X_1} G_{X,m}^{(0)}(\Lambda), \dots, \partial_{X_{n_X}} G_{X,m}^{(0)}(\Lambda), \partial_{Y_1} G_{X,m}^{(0)}(\Lambda), \dots, \partial_{Y_{n_Y}} G_{X,m}^{(0)}(\Lambda) \right).$$

which is a vector in $\mathbb{R}^{1 \times (n_X+n_Y)}$. Note that because $G_{X,m}^{(0)}$ is scalar-valued, the vec operator does nothing, and the resulting derivative is the gradient of $G_{X,m}^{(0)}$. Recall that

$$\Delta\Xi = \left([\psi_X g_X^{(1)} + \psi_X^2 g_X^{(2)} + \dots]^\top, [\psi_Y g_Y^{(1)} + \psi_Y^2 g_Y^{(2)} + \dots]^\top \right)^\top$$

is a column vector. If we denote $g_i^{(\ell)}$ using the vector

$$g_i^{(\ell)} = \begin{pmatrix} g_{i,1}^{(\ell)} \\ g_{i,2}^{(\ell)} \\ \vdots \\ g_{i,n_i}^{(\ell)} \end{pmatrix},$$

then $\Delta\Xi$ can be written,

$$\Delta\Xi = \begin{pmatrix} \psi_X g_{X,1}^{(1)} + \psi_X^2 g_{X,1}^{(2)} + \dots \\ \psi_X g_{X,2}^{(1)} + \psi_X^2 g_{X,2}^{(2)} + \dots \\ \vdots \\ \psi_X g_{X,n_X}^{(1)} + \psi_X^2 g_{X,n_X}^{(2)} + \dots \\ \psi_Y g_{Y,1}^{(1)} + \psi_Y^2 g_{Y,1}^{(2)} + \dots \\ \psi_Y g_{Y,2}^{(1)} + \psi_Y^2 g_{Y,2}^{(2)} + \dots \\ \vdots \\ \psi_Y g_{Y,n_X}^{(1)} + \psi_Y^2 g_{Y,n_X}^{(2)} + \dots \end{pmatrix}$$

It then follows that

$$\begin{aligned} G_{X,m}^{(1)}(\Lambda)\Delta\Xi &= \partial_{X_{n_X}} G_{X,m}^{(0)}(\Lambda) \left[\psi_X g_{X,1}^{(1)} + \psi_X^2 g_{X,1}^{(2)} + \dots \right] + \dots \\ &\quad + \partial_{X_{n_X}} G_{X,m}^{(0)}(\Lambda) \left[\psi_X g_{X,n_X}^{(1)} + \psi_X^2 g_{X,n_X}^{(2)} + \dots \right] \\ &\quad + \partial_{Y_1} G_{X,m}^{(0)}(\Lambda) \left[\psi_Y g_{Y,1}^{(1)} + \psi_Y^2 g_{Y,1}^{(2)} + \dots \right] + \dots \\ &\quad + \partial_{Y_{n_Y}} G_{X,m}^{(0)}(\Lambda) \left[\psi_Y g_{Y,n_X}^{(1)} + \psi_Y^2 g_{Y,n_X}^{(2)} + \dots \right]. \end{aligned}$$

To finish collecting all order ψ^2 terms, we examine the next term,

$$\frac{1}{2} \left[\otimes^2 \Delta\Xi^\top \right] \text{vec} \left(G_{X,m}^{(2)}(\Lambda) \right).$$

The derivative $G_{X,m}^{(2)}(\Lambda)$, given by,

$$\frac{\partial \text{vec} \left(G_{X,m}^{(1)}(\Lambda) \right)}{\partial \Lambda^\top},$$

transposes the first derivative $G_{X,m}^{(1)}$ into a column vector (because it stacks the columns of the row vector) before taking the gradient of each element. We thus end up with the following matrix for $G_{X,m}^{(2)}(\Lambda)$:

$$\begin{pmatrix} \partial_{X_1} \partial_{X_1} G_{X,m}^{(1)}, \dots, \partial_{X_n} \partial_{X_1} G_{X,m}^{(1)}, \partial_{Y_1} \partial_{X_1} G_{X,m}^{(1)}, \dots, \partial_{Y_{n_Y}} \partial_{X_1} G_{X,m}^{(1)} \\ \vdots \\ \partial_{X_1} \partial_{X_{n_X}} G_{X,m}^{(1)}(\Lambda), \dots, \partial_{X_{n_X}} \partial_{X_{n_X}} G_{X,m}^{(1)}, \partial_{Y_1} \partial_{X_{n_X}} G_{X,m}^{(1)}, \dots, \partial_{Y_{n_Y}} \partial_{X_{n_X}} G_{X,m}^{(1)} \\ \partial_{X_1} \partial_{Y_1} G_{X,m}^{(1)}(\Lambda), \dots, \partial_{X_{n_X}} \partial_{Y_1} G_{X,m}^{(1)}, \partial_{Y_1} \partial_{Y_1} G_{X,m}^{(1)}, \dots, \partial_{Y_{n_Y}} \partial_{Y_1} G_{X,m}^{(1)} \\ \vdots \\ \partial_{X_1} \partial_{Y_{n_Y}} G_{X,m}^{(1)}(\Lambda), \dots, \partial_{X_{n_X}} \partial_{Y_{n_Y}} G_{X,m}^{(1)}, \partial_{Y_1} \partial_{Y_{n_Y}} G_{X,m}^{(1)}, \dots, \partial_{Y_{n_Y}} \partial_{Y_{n_Y}} G_{X,m}^{(1)} \end{pmatrix}$$

which is $(n_X + n_Y) \times (n_X + n_Y)$. We then apply the vec operator to this matrix to transform it into a large column vector with $(n_X + n_Y)^2$ elements before taking its dot

product with $\overset{2}{\otimes} \Delta\Xi^\top$, which is given by the large row vector,

$$\overset{2}{\otimes} \Delta\Xi^\top = \begin{pmatrix} [\psi_X g_{X,1}^{(1)} + \dots] \Delta\Xi \\ [\psi_X g_{X,2}^{(1)} + \dots] \Delta\Xi \\ \vdots \\ [\psi_X g_{X,n_X}^{(1)} + \dots] \Delta\Xi \\ [\psi_Y g_{Y,1}^{(1)} + \dots] \Delta\Xi \\ [\psi_Y g_{Y,2}^{(1)} + \dots] \Delta\Xi \\ \vdots \\ [\psi_Y g_{Y,n_Y}^{(1)} + \dots] \Delta\Xi \end{pmatrix}^\top,$$

which rightly has $(n_X + n_Y)^2$ elements. Note that each $\Delta\Xi$ vector is of order $O(\psi_i)$, therefore $\overset{2}{\otimes} \Delta\Xi^\top$ is of order $O(\psi_i^2)$.

Due to the great number of terms involved, we rely on a symbolic solver to handle the collection of terms. In the main body, we simply abbreviate plugging in the ε -expansion of ψ_i ($\psi_i = \varepsilon p_i^{(1)} + \varepsilon^2 p_i^{(2)} + \dots$) by writing

$$\begin{aligned} G_X(\theta_X, \psi_X, \theta_Y, \psi_Y) &= K_X^{(0)}(\theta_X, \theta_Y) + \varepsilon K_X^{(1)}\left(\theta_X, \theta_Y, p_X^{(1)}, p_Y^{(1)}\right) \\ &\quad + \varepsilon^2 K_X^{(2)}\left(\theta_X, \theta_Y, p_X^{(1)}, p_X^{(2)}, p_Y^{(1)}, p_Y^{(2)}\right) \\ &\quad + \varepsilon^3 K_X^{(3)}\left(\theta_X, \theta_Y, p_X^{(1)}, p_X^{(2)}, p_X^{(3)}, p_Y^{(1)}, p_Y^{(2)}, p_Y^{(3)}\right) \\ &\quad + \dots. \end{aligned}$$

Each $K_X^{(\ell)}$ function contains the Floquet eigenfunctions and the partials of G_X . It is straightforward to verify using a symbolic package that the function $K_X^{(\ell)}$ only depends on terms $p_X^{(\ell)}, p_Y^{(\ell)}$ for $\ell \leq k$.

C Phase Estimation

We briefly describe the phase estimation method used in the paper (which is very similar to the estimation done in [31, 34]). Consider a model with state variables x_1, \dots, x_n , and suppose that we have saved a T -periodic limit cycle trajectory (at $\varepsilon = 0$) to some array $[y_1, \dots, y_n]$. Then for a given simulation, we can define the phase to be a point $\theta \in [0, T]$ that minimizes

$$\text{dist}(x_1(t) - y_1(\theta), \dots, x_n(t) - y_n(\theta)),$$

where

$$\text{dist}(\Delta x_1, \dots, \Delta x_n) := \sqrt{(\Delta x_1)^2 + \dots + (\Delta x_n)^2}.$$

By simulating nondimensionalized versions of the equations, we need not normalize by the variance as in [31]. This method is efficient with vectorization.

D Convolution

Recall the $p_X^{(1)}$ term,

$$p_X^{(1)}(\theta_X, \theta_Y) = \omega \int_0^\infty e^{\omega \kappa_X r} I_X^{(0)}(\theta_X - \omega r) \cdot \hat{K}_X^{(0)}(\theta_X - r\omega, \theta_Y - r) dr.$$

The numerical computation of this term can be performed efficiently by utilizing a 1D convolution. The transformation is performed by fixing some $c \in [0, 2\pi)$ such that $\theta_X = c + \theta_Y \omega$. Let H be the Heaviside function. Then,

$$\begin{aligned} p_X^{(1)}(c + \theta_Y \omega, \theta_Y) &= \omega \int_0^\infty e^{\omega \kappa_X r} I_X^{(0)}(c + \omega(\theta_Y - r)) \cdot \hat{K}_X^{(0)}(c + \omega(\theta_Y - r), \theta_Y - r) dr \\ &= \omega \int_{-\infty}^\infty H(r) e^{\omega \kappa_X r} I_X^{(0)}(c + \omega(\theta_Y - r)) \cdot \hat{K}_X^{(0)}(c + \omega(\theta_Y - r), \theta_Y - r) dr \\ &= \omega [H(\theta_Y) e^{\omega \kappa_X \theta_Y}] * f_{X,c}(\theta_Y), \end{aligned}$$

where $f_{X,c}(\theta_Y) = I_X^{(0)}(c + \omega \theta_Y) \cdot \hat{K}_X^{(0)}(c + \omega \theta_Y, \theta_Y)$, and $*$ is the convolution operator. Similarly,

$$p_Y^{(1)}(c + \theta_Y \omega, \theta_Y) = [H(\theta_Y) e^{\kappa_Y \theta_Y}] * f_{Y,c}(\theta_Y),$$

where $f_{Y,c}(\theta_Y) = I_Y^{(0)}(c + \omega \theta_Y) \cdot \hat{K}_Y^{(0)}(c + \omega \theta_Y, \theta_Y)$. Thus, obtaining $p_X^{(1)}(\theta_X, \theta_Y)$ is a matter of transforming the first coordinate.

E Fourier Series

For all functions in this section, assume $x \in [0, 2\pi n)$.

E.1 Nonradial Isochron Clock

The forced nonradial isochron clock in Section 4.1.1 has the following \mathcal{H} functions.

$$\begin{aligned} \mathcal{H}_{1,1}^{(1)}(x) &= -0.3296 \cos(x) + 0.2196 \sin(x), \\ \mathcal{H}_{1,1}^{(2)}(x) &= 0.0272 + 7.2584 \cos(x) + 3.172 \sin(x) + 0.4926 \sin(2x), \\ \mathcal{H}_{2,1}^{(1)}(x) &= -0.1556 \cos(2x) + 0.1038 \sin(2x), \\ \mathcal{H}_{2,1}^{(2)}(x) &= 0.1052 + 0.5916 \cos(2x) + 3.6946 \sin(2x) + 0.1136 \sin(4x), \\ \mathcal{H}_{3,1}^{(1)}(x) &= -0.0446 \cos(3x) + 0.0298 \sin(3x), \\ \mathcal{H}_{3,1}^{(2)}(x) &= 0.0788 - 0.7992 \cos(3x) + 0.7146 \sin(3x) + 0.0094 \sin(6x), \\ \mathcal{H}_{4,1}^{(1)}(x) &= -0.0078 \cos(4x) + 0.0052 \sin(4x), \\ \mathcal{H}_{4,1}^{(2)}(x) &= 0.0544 - 0.1796 \cos(4x) - 0.0498 \sin(4x). \end{aligned}$$

E.2 Forced Thalamic Oscillator

$$\begin{aligned}
\mathcal{H}_{1,1}^{(1)}(x) &= 1.2816 \sin(x) + 0.0746 \sin(2x) - 0.014 \sin(3x) - 0.0018 \sin(4x) \\
&\quad + 1.1556 \cos(1x) + 0.1188 \cos(2x) + 0.014 \cos(3x) + 0.001 \cos(4x) \\
\mathcal{H}_{1,1}^{(2)}(x) &= 9.6616 \cos(1x) + 1.8382 \cos(2x) + 0.466 \cos(3x) + 0.0608 \cos(4x) \\
&\quad - 0.0046 \cos(5x) - 0.0004 \cos(6x) + 2.2889 - 32.8754 \sin(x) \\
&\quad - 3.9426 \sin(2x) - 0.8276 \sin(3x) - 0.0028 \sin(4x) - 0.0024 \sin(5x) \\
&\quad - 0.0022 \sin(6x) - 0.0004 \sin(7x), \\
\mathcal{H}_{2,1}^{(1)}(x) &= 0.6054 \sin(2x) + 0.0038 \sin(4x) + 0.5458 \cos(2x) + 0.006 \cos(4x), \\
\mathcal{H}_{2,1}^{(2)}(x) &= -4.8458 \sin(2x) - 0.3894 \sin(4x) - 0.011 \sin(6x) + 15.5844 \cos(2x) \\
&\quad - 0.0916 \cos(4x) + 0.005 \cos(6x) + 0.533, \\
\mathcal{H}_{1,2}^{(1)}(x) &= 0.1578 \sin(2x) - 0.038 \sin(4x) - 0.0024 \sin(6x) + 0.2514 \cos(2x) \\
&\quad + 0.0194 \cos(4x) - 0.0012 \cos(6x) - 0.0002 \cos(8x), \\
\mathcal{H}_{1,2}^{(2)}(x) &= -0.1508 \cos(2x) - 0.2636 \cos(4x) - 0.0728 \cos(6x) + 0.0468 \\
&\quad - 5.93 \sin(2x) - 0.8184 \sin(4x) - 0.1026 \sin(6x) \\
&\quad - 0.01 \sin(8x) - 0.0006 \sin(10x) - 0.0062 \cos(8x) - 0.001 \cos(10x), \\
\mathcal{H}_{2,3}^{(1)}(x) &= -0.0486 \sin(6x) - 0.0004 \sin(12x) + 0.0488 \cos(6x) - 0.0002 \cos(12x), \\
\mathcal{H}_{2,3}^{(2)}(x) &= -1.2122 \sin(6x) - 0.0224 \sin(12x) - 0.0004 \sin(18x) - 0.4998 \cos(6x) \\
&\quad + 0.0154 \cos(12x) - 0.0766.
\end{aligned}$$

E.3 Coupled Thalamic Oscillators

In this section, denote the heterogeneous term of $O(\varepsilon)$ by $\mathcal{J}_i^{(1)}$ (denoted $b\mathcal{J}_i$ in Figures 13 through 21), and the heterogeneous term of $O(\varepsilon^2)$ by $\mathcal{J}_i^{(2,\ell)}$ for $\ell = 1, 2$ (denoted $b^2\mathcal{J}_i$ in Figures 13 through 21).

E.3.1 1:1

Plots of the following \mathcal{H} and \mathcal{J} functions are shown in Figure 13.

$$\begin{aligned}
\mathcal{H}_X^{(1)} &= 0.2342 - 0.2549 \cos(x) - 0.0167 \cos(2x) + 0.0092 \cos(3x) \\
&\quad + 0.0050 \cos(4x) + 0.0020 \cos(5x) - 0.0646 \sin(x) + 0.0095 \sin(3x) \\
&\quad + 0.0038 \sin(4x) \\
\mathcal{J}_X^{(1)} &= -5.9757 \\
\mathcal{H}_X^{(2)} &= 0.1225 + 0.0198 \cos(x) - 0.1412 \cos(2x) - 0.0335 \cos(3x) \\
&\quad + 0.0161 \cos(4x) + 0.0114 \cos(5x) + 0.0035 \cos(6x) + 0.0044 \sin(x) \\
&\quad - 0.0393 \sin(2x) - 0.0098 \sin(3x) + 0.0130 \sin(4x) + 0.0089 \sin(5x) \\
\mathcal{J}_X^{(2,1)} &= -0.1329 + 0.3773 \cos(x) + 0.0519 \cos(2x) - 0.1553 \cos(3x) \\
&\quad - 0.0872 \cos(4x) - 1.5871 \sin(x) - 0.2154 \sin(2x) + 0.1683 \sin(3x) \\
&\quad + 0.1167 \sin(4x) + 0.0569 \sin(5x) + 0.0276 \sin(6x) \\
\mathcal{J}_X^{(2,2)} &= -595.9792 \\
\mathcal{H}_Y^{(1)} &= 0.2342 - 0.2549 \cos(x) - 0.0167 \cos(2x) + 0.0092 \cos(3x) \\
&\quad + 0.0050 \cos(4x) + 0.0020 \cos(5x) + 0.0646 \sin(x) - 0.0095 \sin(3x) \\
&\quad - 0.0038 \sin(4x) \\
\mathcal{J}_Y^{(1)} &= 0 \\
\mathcal{H}_Y^{(2)} &= 0.1225 + 0.0198 \cos(x) - 0.1412 \cos(2x) - 0.0335 \cos(3x) \\
&\quad + 0.0161 \cos(4x) + 0.0114 \cos(5x) + 0.0035 \cos(6x) - 0.0044 \sin(x) \\
&\quad + 0.0393 \sin(2x) + 0.0098 \sin(3x) - 0.0130 \sin(4x) - 0.0089 \sin(5x) \\
\mathcal{J}_Y^{(2,1)} &= -0.3363 \cos(x) + 0.1566 \cos(3x) + 0.0843 \cos(4x) \\
&\quad - 1.4361 \sin(x) - 0.1853 \sin(2x) + 0.1536 \sin(3x) + 0.1112 \sin(4x) \\
&\quad + 0.0559 \sin(5x) + 0.0274 \sin(6x) \\
\mathcal{J}_Y^{(2,2)} &= 0
\end{aligned}$$

E.3.2 1:2

Plots of the following \mathcal{H} and \mathcal{J} functions are shown in Figure 14.

$$\begin{aligned}
\mathcal{H}_X^{(1)} &= 0.2342 - 0.0208 \cos(2x) + 0.0067 \cos(4x) + 0.0021 \cos(6x) \\
&\quad - 0.0070 \sin(2x) + 0.0093 \sin(4x) \\
\mathcal{J}_X^{(1)} &= -5.9757 \\
\mathcal{H}_X^{(2)} &= 0.0068 - 0.0105 \cos(2x) + 0.0049 \cos(4x) - 0.0026 \cos(6x) \\
&\quad + 0.0081 \sin(2x) - 0.0091 \sin(4x) + 0.0051 \sin(6x) \\
\mathcal{J}_X^{(2,1)} &= -0.1329 + 0.1519 \cos(2x) - 0.2134 \cos(4x) + 0.0251 \cos(8x) \\
&\quad - 0.2476 \sin(2x) + 0.1569 \sin(4x) + 0.0697 \sin(6x) + 0.0246 \sin(8x) \\
\mathcal{J}_X^{(2,2)} &= -595.9792 \\
\mathcal{H}_Y^{(1)} &= 0.2342 - 0.2001 \cos(2x) - 0.0088 \cos(4x) + 0.0045 \cos(6x) \\
&\quad - 0.0132 \sin(2x) - 0.0026 \sin(4x) - 0.0031 \sin(6x) \\
\mathcal{J}_Y^{(1)} &= 0 \\
\mathcal{H}_Y^{(2)} &= 0.0368 - 0.0303 \cos(4x) - 0.0059 \cos(6x) + 0.0035 \cos(8x) \\
&\quad + 0.0358 \sin(2x) - 0.0400 \sin(4x) + 0.0022 \sin(6x) + 0.0024 \sin(8x) \\
\mathcal{J}_Y^{(2,1)} &= 0.1786 \cos(2x) + 0.0576 \cos(4x) + 0.1024 \cos(6x) \\
&\quad + 0.0450 \cos(8x) - 2.2168 \sin(2x) - 0.1944 \sin(4x) + 0.1486 \sin(6x) \\
&\quad + 0.0670 \sin(8x) \\
\mathcal{J}_Y^{(2,2)} &= 0
\end{aligned}$$

E.3.3 2:1

Plots of the following \mathcal{H} and \mathcal{J} functions are shown in Figure 15.

$$\begin{aligned}
\mathcal{H}_X^{(1)} &= 0.2342 - 0.2001 \cos(2x) - 0.0088 \cos(4x) + 0.0045 \cos(6x) \\
&\quad + 0.0132 \sin(2x) + 0.0026 \sin(4x) + 0.0031 \sin(6x) \\
\mathcal{J}_X^{(1)} &= -5.9757 \\
\mathcal{H}_X^{(2)} &= 0.0368 - 0.0303 \cos(4x) - 0.0059 \cos(6x) + 0.0035 \cos(8x) \\
&\quad - 0.0358 \sin(2x) + 0.0400 \sin(4x) - 0.0022 \sin(6x) - 0.0024 \sin(8x) \\
\mathcal{J}_X^{(2,1)} &= -0.1346 - 0.1011 \cos(2x) - 0.0490 \cos(6x) - 0.0230 \cos(8x) \\
&\quad - 1.2527 \sin(2x) - 0.1229 \sin(4x) + 0.0814 \sin(6x) + 0.0356 \sin(8x) \\
\mathcal{J}_X^{(2,2)} &= -595.9595 \\
\mathcal{H}_Y^{(1)} &= 0.2342 - 0.0208 \cos(2x) + 0.0067 \cos(4x) + 0.0021 \cos(6x) \\
&\quad + 0.0070 \sin(2x) - 0.0093 \sin(4x) \\
\mathcal{J}_Y^{(1)} &= 0 \\
\mathcal{H}_Y^{(2)} &= 0.0068 - 0.0105 \cos(2x) + 0.0049 \cos(4x) - 0.0026 \cos(6x) \\
&\quad - 0.0081 \sin(2x) + 0.0091 \sin(4x) - 0.0051 \sin(6x) \\
\mathcal{J}_Y^{(2,1)} &= -0.0373 \cos(2x) + 0.1034 \cos(4x) - 0.1184 \sin(2x) \\
&\quad + 0.0769 \sin(4x) + 0.0346 \sin(6x) \\
\mathcal{J}_Y^{(2,2)} &= 0
\end{aligned}$$

E.3.4 1:3

Plots of the following \mathcal{H} and \mathcal{J} functions are shown in Figure 16.

$$\begin{aligned}
\mathcal{H}_X^{(1)} &= 0.2342 + 0.0062 \cos(3x) + 0.0028 \cos(6x) + 0.0226 \sin(3x) \\
\mathcal{J}_X^{(1)} &= -5.9757 \\
\mathcal{H}_X^{(2)} &= 0.0126 \cos(3x) - 0.0027 \sin(6x) \\
\mathcal{J}_X^{(2,1)} &= -0.1329 - 0.3844 \cos(3x) + 0.0258 \cos(9x) + 0.1298 \sin(3x) \\
&\quad + 0.0938 \sin(6x) + 0.0245 \sin(9x) \\
\mathcal{J}_X^{(2,2)} &= -595.9792 \\
\mathcal{H}_Y^{(1)} &= 0.2342 - 0.1437 \cos(3x) - 0.0047 \cos(6x) - 0.0370 \sin(3x) \\
\mathcal{J}_Y^{(1)} &= 0 \\
\mathcal{H}_Y^{(2)} &= 0.0093 - 0.0147 \cos(3x) - 0.0020 \cos(6x) - 0.0045 \cos(9x) \\
&\quad + 0.0715 \sin(3x) - 0.0067 \sin(6x) \\
\mathcal{J}_Y^{(2,1)} &= 0.6305 \cos(3x) + 0.0618 \cos(6x) + 0.0634 \cos(9x) \\
&\quad + 0.0250 \cos(12x) - 2.3754 \sin(3x) - 0.1567 \sin(6x) + 0.0736 \sin(9x) \\
\mathcal{J}_Y^{(2,2)} &= 0
\end{aligned}$$

E.3.5 3:1

Plots of the following \mathcal{H} and \mathcal{J} functions are shown in Figure 17.

$$\begin{aligned}
\mathcal{H}_X^{(1)} &= 0.2342 - 0.1437 \cos(3x) - 0.0047 \cos(6x) + 0.0370 \sin(3x) \\
\mathcal{J}_X^{(1)} &= -5.9757 \\
\mathcal{H}_X^{(2)} &= 0.0093 - 0.0147 \cos(3x) - 0.0020 \cos(6x) - 0.0045 \cos(9x) \\
&\quad - 0.0715 \sin(3x) + 0.0067 \sin(6x) \\
\mathcal{J}_X^{(2,1)} &= -0.1349 - 0.2452 \cos(3x) - 0.0203 \cos(9x) - 0.8977 \sin(3x) \\
&\quad - 0.0673 \sin(6x) + 0.0272 \sin(9x) \\
\mathcal{J}_X^{(2,2)} &= -1193.5286 \\
\mathcal{H}_Y^{(1)} &= 0.2342 + 0.0062 \cos(3x) + 0.0028 \cos(6x) - 0.0226 \sin(3x) \\
\mathcal{J}_Y^{(2,1)} &= 0 \\
\mathcal{H}_Y^{(2)} &= 0.0126 \cos(3x) + 0.0027 \sin(6x) \\
\mathcal{J}_Y^{(2,1)} &= 0.1276 \cos(3x) + 0.0375 \sin(3x) + 0.0312 \sin(6x) \\
\mathcal{J}_Y^{(2,2)} &= 0
\end{aligned}$$

E.3.6 2:3

Plots of the following \mathcal{H} and \mathcal{J} functions are shown in Figure 18.

$$\begin{aligned}
\mathcal{H}_X^{(1)} &= 0.2342 + 0.0098 \cos(6x) + 0.0149 \sin(6x) \\
\mathcal{J}_X^{(1)} &= -5.9757 \\
\mathcal{H}_X^{(2)} &= 0.0014 + 0.0075 \cos(6x) - 0.0039 \sin(6x) - 0.0028 \sin(12x) \\
\mathcal{J}_X^{(2,1)} &= -0.1346 - 0.2507 \cos(6x) + 0.1866 \sin(6x) + 0.0516 \sin(12x) \\
\mathcal{J}_X^{(2,2)} &= -11949.8445 \\
\mathcal{H}_Y^{(1)} &= 0.2342 - 0.0122 \cos(6x) + 0.0030 \cos(12x) - 0.0022 \sin(6x) \\
\mathcal{J}_Y^{(1)} &= 0 \\
\mathcal{H}_Y^{(2)} &= 0.0024 + 0.0040 \sin(6x) \\
\mathcal{J}_Y^{(2,1)} &= 0.0378 \cos(6x) + 0.0623 \cos(12x) - 0.2033 \sin(6x) \\
&\quad + 0.0992 \sin(12x) \\
\mathcal{J}_Y^{(2,2)} &= 0
\end{aligned}$$

E.3.7 3:2

Plots of the following \mathcal{H} and \mathcal{J} functions are shown in Figure 19.

$$\begin{aligned}
\mathcal{H}_X^{(1)} &= 0.2342 - 0.0122 \cos(6x) + 0.0030 \cos(12x) + 0.0022 \sin(6x) \\
\mathcal{J}_X^{(1)} &= -5.9757 \\
\mathcal{H}_X^{(2)} &= 0.0024 - 0.0040 \sin(6x) \\
\mathcal{J}_X^{(2,1)} &= -0.1349 - 0.0424 \cos(12x) - 0.1655 \sin(6x) + 0.0695 \sin(12x) \\
\mathcal{J}_X^{(2,2)} &= -11949.8408 \\
\mathcal{H}_Y^{(1)} &= 0.2342 + 0.0098 \cos(6x) - 0.0149 \sin(6x) \\
\mathcal{J}_Y^{(1)} &= 0 \\
\mathcal{H}_Y^{(2)} &= 0.0014 + 0.0075 \cos(6x) + 0.0039 \sin(6x) + 0.0028 \sin(12x) \\
\mathcal{J}_Y^{(2,1)} &= 0.1659 \cos(6x) + 0.1126 \sin(6x) + 0.0339 \sin(12x) \\
\mathcal{J}_Y^{(2,2)} &= 0
\end{aligned}$$

E.3.8 3:4

Plots of the following \mathcal{H} and \mathcal{J} functions are shown in Figure 20.

$$\begin{aligned}
\mathcal{H}_X^{(1)} &= 0.2342 + 0.0062 \cos(12x) + 0.0059 \sin(12x) \\
\mathcal{J}_X^{(1)} &= -5.9757 \\
\mathcal{H}_X^{(2)} &= 0.0035 \cos(12x) - 0.0040 \sin(12x) \\
\mathcal{J}_X^{(2,1)} &= -0.1349 - 0.1352 \cos(12x) + 0.1448 \sin(12x) \\
\mathcal{J}_X^{(2,2)} &= -5974.1118 \\
\mathcal{H}_Y^{(1)} &= 0.2342 + 0.0076 \cos(12x) - 0.0063 \sin(12x) \\
\mathcal{J}_Y^{(1)} &= 0 \\
\mathcal{H}_Y^{(2)} &= 0.0049 - 0.0030 \cos(12x) \\
\mathcal{J}_Y^{(2,1)} &= 0.1398 \cos(12x) + 0.1691 \sin(12x) \\
\mathcal{J}_Y^{(2,2)} &= 0
\end{aligned}$$

E.3.9 4:3

Plots of the following \mathcal{H} and \mathcal{J} functions are shown in Figure 21.

$$\begin{aligned}
\mathcal{H}_X^{(1)} &= 0.2342 + 0.0076 \cos(12x) + 0.0063 \sin(12x) \\
\mathcal{J}_X^{(1)} &= -5.9757 \\
\mathcal{H}_X^{(2)} &= 0.0049 - 0.0030 \cos(12x) \\
\mathcal{J}_X^{(2,1)} &= -0.1352 - 0.1020 \cos(12x) + 0.1385 \sin(12x) \\
\mathcal{J}_X^{(2,2)} &= -5974.1083 \\
\mathcal{H}_Y^{(1)} &= 0.2342 + 0.0062 \cos(12x) - 0.0059 \sin(12x) \\
\mathcal{J}_Y^{(1)} &= 0 \\
\mathcal{H}_Y^{(2)} &= 0.0035 \cos(12x) + 0.0040 \sin(12x) \\
\mathcal{J}_Y^{(2,1)} &= 0.0973 \cos(12x) + 0.1039 \sin(12x) \\
\mathcal{J}_Y^{(2,2)} &= 0
\end{aligned}$$

References

- [1] S. ADHIKARI, J. G. RESTREPO, AND P. S. SKARDAL, *Synchronization of phase oscillators on complex hypergraphs*, Chaos: An Interdisciplinary Journal of Nonlinear Science, 33 (2023).
- [2] A. BHASKAR, B. SHAYAK, A. T. ZEHNDER, AND R. H. RAND, *Integer ratio self-synchronization in pairs of limit cycle oscillators*, in International Design Engineering Technical Conferences and Computers and Information in Engineering Conference, vol. 85482, American Society of Mechanical Engineers, 2021, p. V011T11A010.
- [3] R. J. BUTERA JR, J. RINZEL, AND J. C. SMITH, *Models of respiratory rhythm generation in the pre-Bötzinger complex. ii. populations of coupled pacemaker neurons*, Journal of Neurophysiology, 82 (1999), pp. 398–415.
- [4] C. C. CANAVIER, F. G. KAZANCI, AND A. A. PRINZ, *Phase resetting curves allow for simple and accurate prediction of robust N:1 phase locking for strongly coupled neural oscillators*, Biophysical Journal, 97 (2009), pp. 59–73.
- [5] J. CHEN, K. WONG, H. ZHENG, AND J. SHUAI, *Phase signal coupling induced n: m phase synchronization in drive-response oscillators*, Physical Review E, 63 (2001), p. 036214.
- [6] I. R. EPSTEIN AND J. A. POJMAN, *An introduction to nonlinear chemical dynamics: oscillations, waves, patterns, and chaos*, Oxford University Press, 1998.
- [7] G. B. ERMENTROUT, *n:m phase-locking of weakly coupled oscillators*, J. Math. Biol., 12 (1981), pp. 327–342, <https://doi.org/10.1007/BF00276920>.
- [8] G. B. ERMENTROUT, *Simulating, analyzing, and animating dynamical systems: a guide to XPPAUT for researchers and students*, vol. 14, SIAM, 2002.
- [9] G. B. ERMENTROUT AND D. H. TERMAN, *Mathematical foundations of neuroscience*, vol. 35 of Interdisciplinary Applied Mathematics, Springer, New York, 2010, <https://doi.org/10.1007/978-0-387-87708-2>.
- [10] L. GLASS AND R. PEREZ, *Fine structure of phase locking*, Physical Review Letters, 48 (1982), p. 1772.

- [11] E. E. GOLDWYN AND A. HASTINGS, *Small heterogeneity has large effects on synchronization of ecological oscillators*, Bulletin of Mathematical Biology, 71 (2009), pp. 130–144.
- [12] M. GOLUBITSKY AND I. STEWART, *The symmetry perspective: from equilibrium to chaos in phase space and physical space*, vol. 200, Springer Science & Business Media, 2003.
- [13] V. HORVÁTH, D. J. KUTNER, M. D. ZENG, AND I. R. EPSTEIN, *Phase-frequency model of strongly pulse-coupled Belousov-Zhabotinsky oscillators*, Chaos: An Interdisciplinary Journal of Nonlinear Science, 29 (2019), p. 023128, <https://doi.org/10.1063/1.5082161>, <https://doi.org/10.1063/1.5082161>, https://arxiv.org/abs/https://pubs.aip.org/aip/cha/article-pdf/doi/10.1063/1.5082161/14621317/023128\1_online.pdf.
- [14] I. HUNTER, M. M. NORTON, B. CHEN, C. SIMONETTI, M. E. MOUSTAKA, J. TOUBOUL, AND S. FRADEN, *Pattern formation in a four-ring reaction-diffusion network with heterogeneity*, Physical Review E, 105 (2022), p. 024310, <https://doi.org/10.1103/PhysRevE.105.024310>, <https://link.aps.org/doi/10.1103/PhysRevE.105.024310>.
- [15] E. M. IZHIKEVICH, *Dynamical systems in neuroscience: the geometry of excitability and bursting*, Computational Neuroscience, MIT Press, Cambridge, MA, 2007.
- [16] Y. KURAMOTO, *Chemical oscillations, waves, and turbulence*, vol. 19 of Springer Series in Synergetics, Springer-Verlag, Berlin, 1984, <https://doi.org/10.1007/978-3-642-69689-3>.
- [17] J. LENGLER, F. JUG, AND A. STEGER, *Reliable neuronal systems: the importance of heterogeneity*, PloS one, 8 (2013), p. e80694.
- [18] J. LLIBRE, D. D. NOVAES, AND M. A. TEIXEIRA, *Higher order averaging theory for finding periodic solutions via Brouwer degree*, Nonlinearity, 27 (2014), pp. 563–583, <https://doi.org/10.1088/0951-7715/27/3/563>.
- [19] M. MAGGIA, S. A. EISA, AND H. E. TAHA, *On higher-order averaging of time-periodic systems: reconciliation of two averaging techniques*, Nonlinear Dynamics, 99 (2020), pp. 813–836.
- [20] J. R. MAGNUS AND H. NEUDECKER, *Matrix differential calculus with applications in statistics and econometrics*, John Wiley & Sons, 2019.
- [21] E. MARDER, S. KEDIA, AND E. O. MOROZOVA, *New insights from small rhythmic circuits*, Current Opinion in Neurobiology, 76 (2022), p. 102610.
- [22] E. T. MAU, M. ROSENBLUM, AND A. PIKOVSKY, *High-order phase reduction for coupled 2d oscillators*, Chaos: An Interdisciplinary Journal of Nonlinear Science, 33 (2023).
- [23] A. MAUROY, I. MEZIĆ, AND J. MOEHLIS, *Isostables, isochrons, and Koopman spectrum for the action-angle representation of stable fixed point dynamics*, Phys. D, 261 (2013), pp. 19–30.
- [24] J. MCKINLEY, M. ZHANG, A. WEAD, C. WILLIAMS, E. TOGNOLI, AND C. BEEBLE, *Third party stabilization of unstable coordination in systems of coupled oscillators*, in Journal of Physics: Conference Series, vol. 2090, IOP Publishing, 2021, p. 012167.
- [25] I. MEZIĆ, *Spectrum of the koopman operator, spectral expansions in functional spaces, and state-space geometry*, J. Nonlinear. Sci., 30 (2020), pp. 2091–2145.

[26] R. MILNE AND F. GUICHARD, *Coupled phase-amplitude dynamics in heterogeneous metacommunities*, Journal of Theoretical Biology, 523 (2021), p. 110676.

[27] R. E. MIROLLO AND S. H. STROGATZ, *Synchronization of pulse-coupled biological oscillators*, SIAM J. Appl. Math., 50 (1990), pp. 1645–1662, <https://doi.org/10.1137/0150098>.

[28] R. NICKS, R. ALLEN, AND S. COOMBES, *Insights into oscillator network dynamics using a phase-isostable framework*, Chaos: An Interdisciplinary Journal of Nonlinear Science, 34 (2024).

[29] M. M. NORTON, N. TOMPKINS, B. BLANC, M. C. CAMBRIA, J. HELD, AND S. FRADEN, *Dynamics of reaction-diffusion oscillators in star and other networks with cyclic symmetries exhibiting multiple clusters*, Physical review letters, 123 (2019), p. 148301.

[30] E. OTT AND T. M. ANTONSEN, *Low dimensional behavior of large systems of globally coupled oscillators*, Chaos, 18 (2008), p. 037113.

[31] Y. PARK AND G. B. ERMENTROUT, *Weakly coupled oscillators in a slowly varying world*, J. Journal of Computational Neuroscience, 40 (2016), pp. 269–281, <https://doi.org/10.1007/s10827-016-0596-6>.

[32] Y. PARK, S. HEITMANN, AND G. B. ERMENTROUT, *The utility of phase models in studying neural synchronization*, in Computational Models of Brain and Behavior, A. A. Moustafa, ed., Wiley Online Library, 2017, ch. 36, pp. 493–504.

[33] Y. PARK AND D. WILSON, *High-order accuracy computation of coupling functions for strongly coupled oscillators*, SIAM Journal on Applied Dynamical Systems, 20 (2021), pp. 1464–1484.

[34] Y. PARK AND D. WILSON, *N-body oscillator interactions of higher-order coupling functions*, SIAM Journal on Applied Dynamical Systems, 23 (2024), pp. 1471–1503.

[35] A. PÉREZ-CERVERA, T. M. SEARA, AND G. HUGUET, *Global phase-amplitude description of oscillatory dynamics via the parameterization method*, arXiv preprint arXiv:2004.03647, (2020).

[36] M. ROSENBLUM AND A. PIKOVSKY, *Numerical phase reduction beyond the first order approximation*, Chaos, 29 (2019), p. 011105.

[37] J. E. RUBIN AND D. TERMAN, *High frequency stimulation of the subthalamic nucleus eliminates pathological thalamic rhythmicity in a computational model*, Journal of Computational Neuroscience, 16 (2004), pp. 211–235.

[38] M. A. SCHWEMMER AND T. J. LEWIS, *The theory of weakly coupled oscillators*, in Phase response curves in neuroscience: theory, experiment, and analysis, Springer, 2011, pp. 3–31.

[39] S. SHIRASAKA, W. KUREBAYASHI, AND H. NAKAO, *Phase-amplitude reduction of transient dynamics far from attractors for limit-cycling systems*, Chaos, 27 (2017), p. 023119.

[40] R. B. STEIN, E. R. GOSSEN, AND K. E. JONES, *Neuronal variability: noise or part of the signal?*, Nature Reviews Neuroscience, 6 (2005), pp. 389–397.

[41] S. H. STROGATZ, D. M. ABRAMS, A. McROBIE, B. ECKHARDT, AND E. OTT, *Crowd synchrony on the millennium bridge*, Nature, 438 (2005), pp. 43–44.

[42] N. URBAN AND S. TRIPATHY, *Circuits drive cell diversity*, Nature, 488 (2012), pp. 289–290.

- [43] K. C. A. WEDGWOOD, K. K. LIN, R. THUL, AND S. COOMBES, *Phase-amplitude descriptions of neural oscillator models*, J. Math. Neurosci., 3 (2013), p. 2.
- [44] D. WILSON. Personal communication.
- [45] D. WILSON, *Phase-amplitude reduction far beyond the weakly perturbed paradigm*, Physical Review E, 101 (2020), p. 022220.
- [46] D. WILSON AND G. B. ERMENTROUT, *Greater accuracy and broadened applicability of phase reduction using isostable coordinates*, J. Math. Biol., 76 (2018), pp. 37–66, <https://doi.org/10.1007/s00285-017-1141-6>.
- [47] D. WILSON AND G. B. ERMENTROUT, *An operational definition of phase characterizes the transient response of perturbed limit cycle oscillators*, SIAM J. Appl. Dyn. Syst., 17 (2018), pp. 2516–2543.
- [48] D. WILSON AND G. B. ERMENTROUT, *Phase models beyond weak coupling*, Phys. Rev. Lett., 123 (2019), p. 164101.
- [49] D. WILSON AND J. MOEHLIS, *Isostable reduction of periodic orbits*, Phys. Rev. E, 94 (2016), p. 052213.
- [50] A. T. WINFREE, *The geometry of biological time*, vol. 12, Springer Science & Business Media, 2001.
- [51] Y. ZANG AND E. MARDER, *Neuronal morphology enhances robustness to perturbations of channel densities*, Proceedings of the National Academy of Sciences, 120 (2023), p. e2219049120.

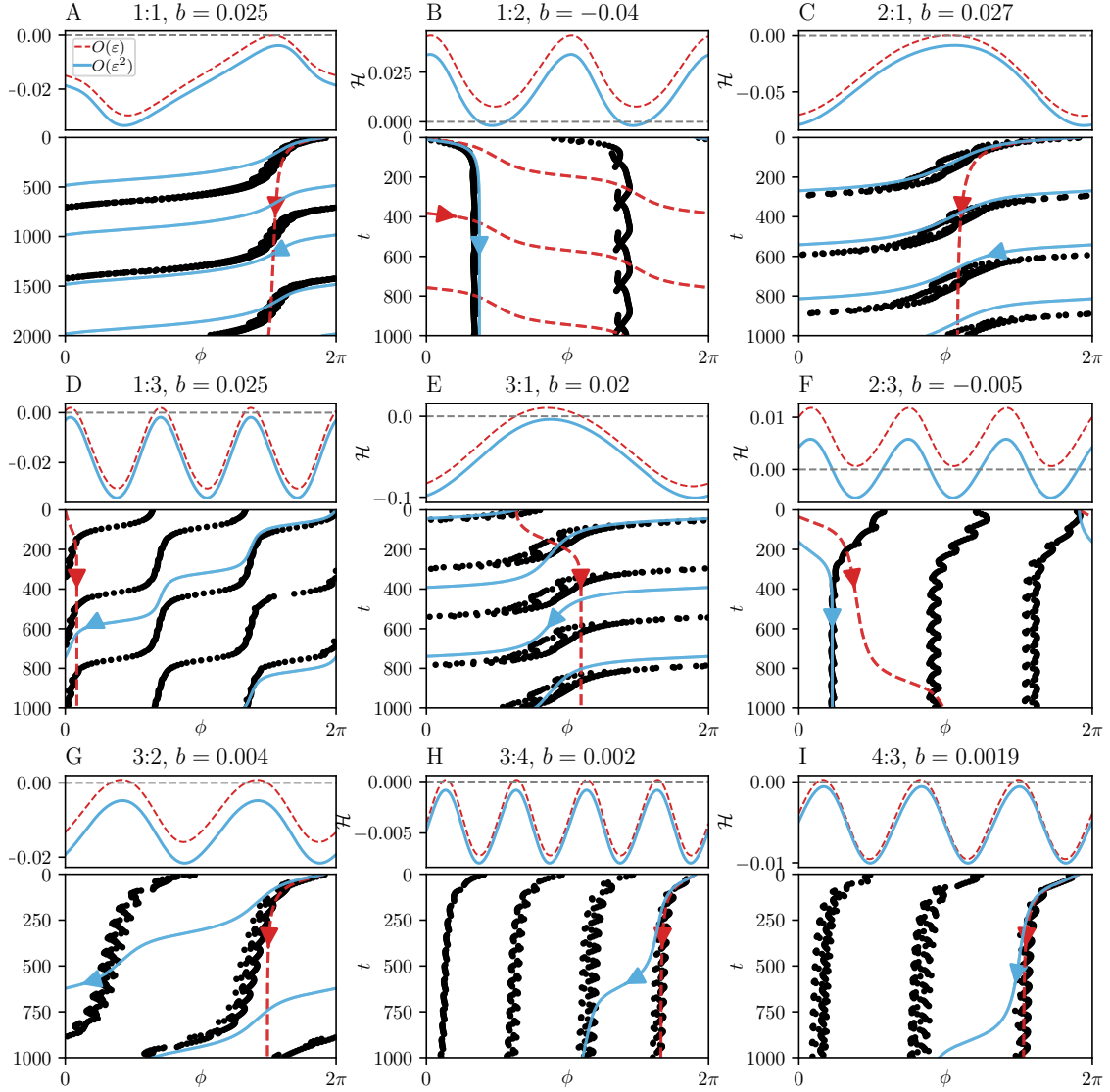


Figure 8: Representative trajectories of the scalar reduction (red dashed for order $O(\varepsilon)$ and blue for order $O(\varepsilon^2)$) compared to the original coupled thalamic models (black) for various degrees of heterogeneity b . The coupling strength ε is chosen to be $\varepsilon = 0.1$ for panels. We choose $c_1 = 1$ for all panels and $c_2 = [100, 100, 100, 100, 200, 2000, 2000, 1000, 1000]$ for respective panels A through I. Only one every two hundredth point of the full model's phase difference estimate is displayed, to reduce lag when loading the figure.

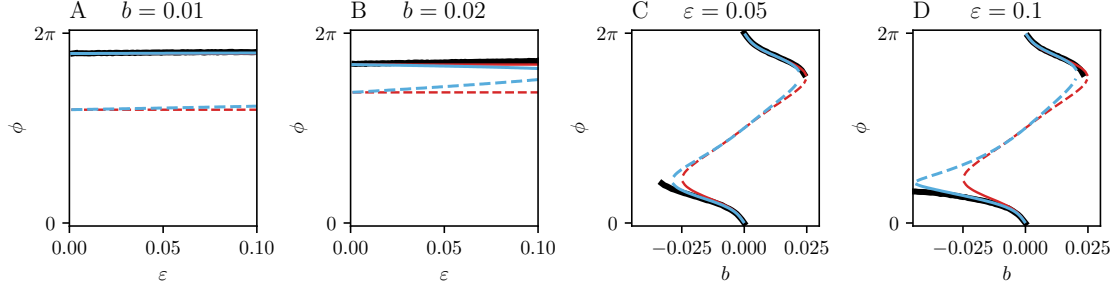


Figure 9: One-parameter bifurcation diagrams for 1:1 phase-locking in a pair of thalamic neurons given varying levels of heterogeneity. All panels show the existence of fixed points in the $O(\varepsilon)$ reduction (red), $O(\varepsilon^2)$ reduction (blue), and full model (black). Solid (dashed) curves correspond to stable (unstable) fixed points. Panels A, B show bifurcation diagrams as a function of coupling strength ε given heterogeneity $b = 0.01$ (A) and $b = 0.02$ (B). Panels C, D show bifurcation diagrams as a function of heterogeneity b given coupling strengths $\varepsilon = 0.05$ (C) and $\varepsilon = 0.1$ (D). One-parameter bifurcations for remaining phase-locking combinations in Figure 8 are shown in Figures 10 and 11.

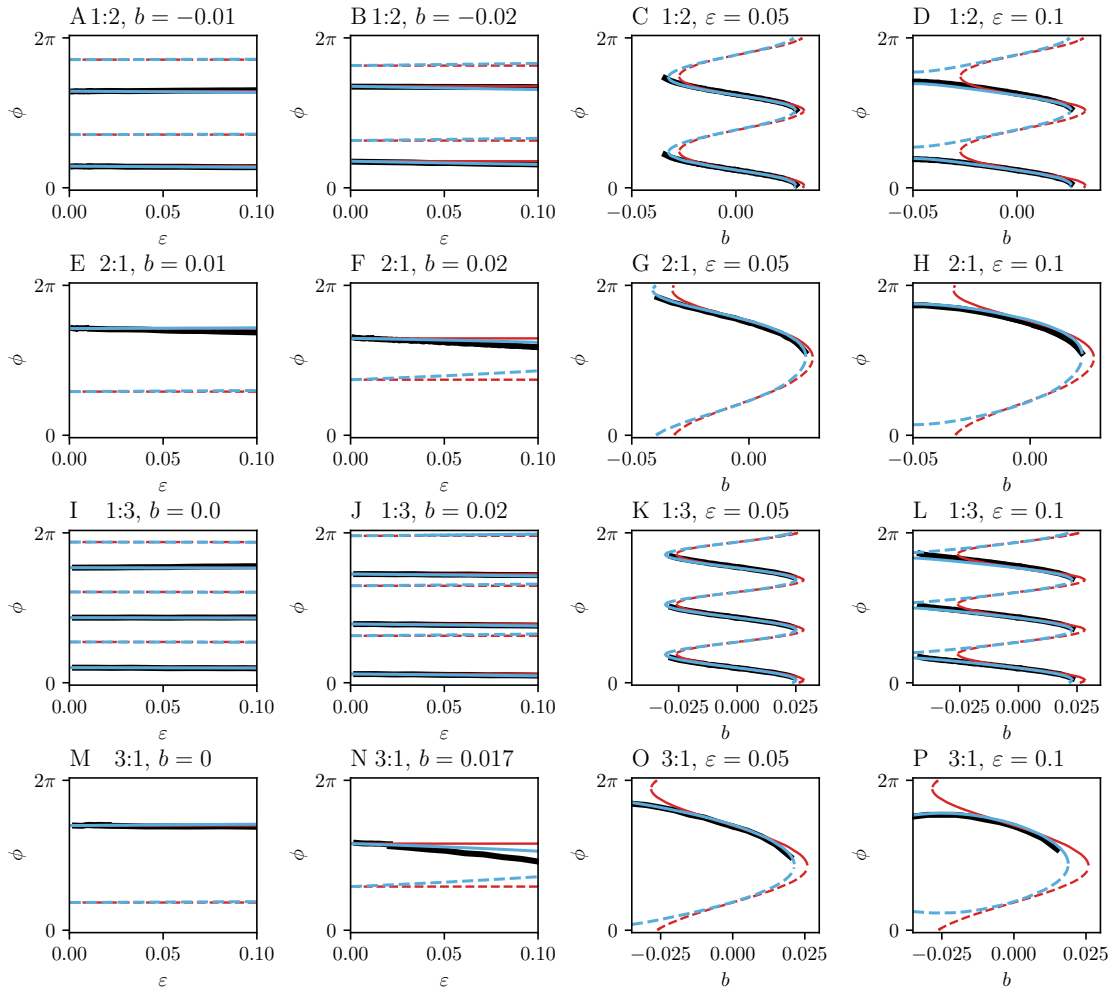


Figure 10: One-parameter bifurcation diagrams for $n:m$ phase-locking in a pair of thalamic neurons given varying levels of heterogeneity. All panels show the existence of fixed points in the $O(\varepsilon)$ reduction (red), $O(\varepsilon^2)$ reduction (blue), and full model (black). Solid (dashed) curves correspond to stable (unstable) fixed points.

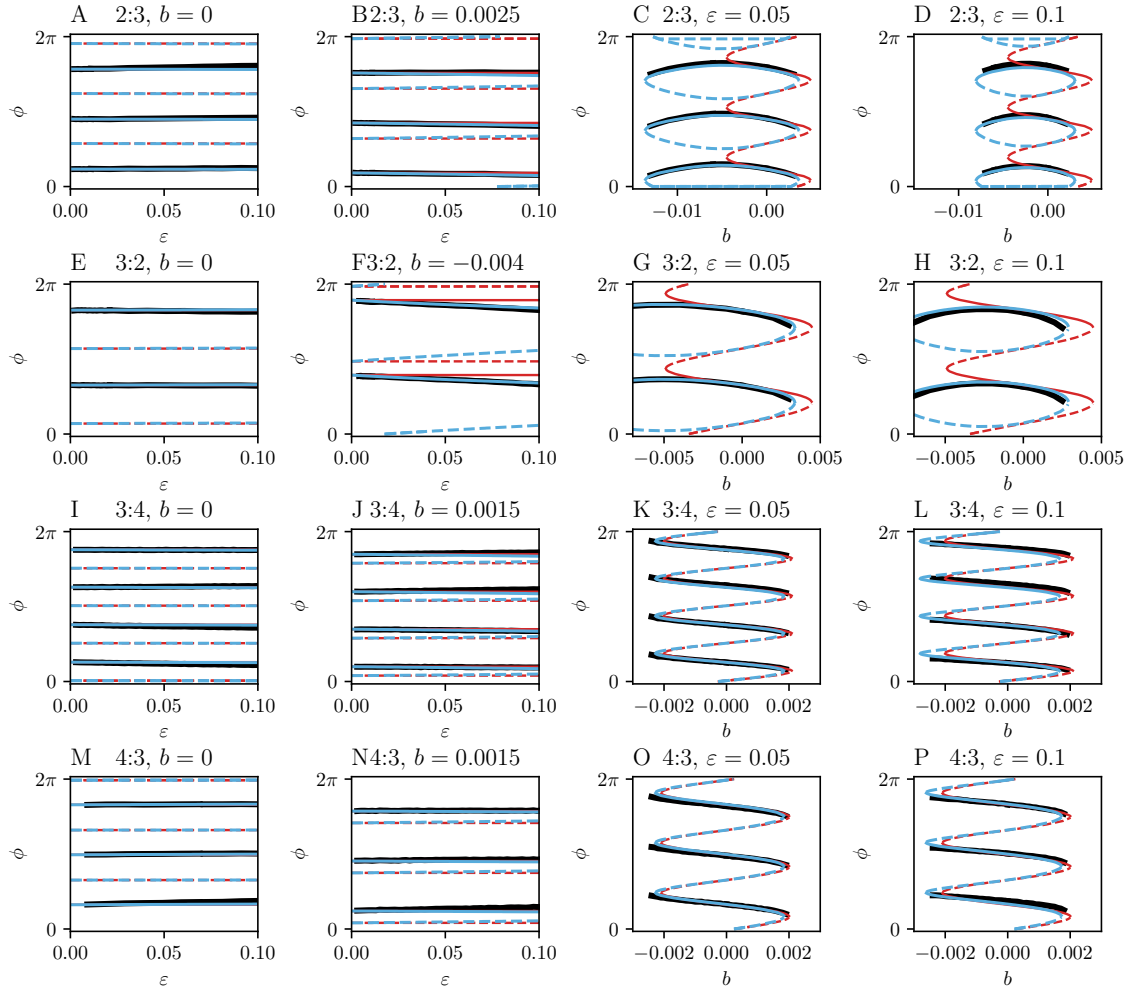


Figure 11: One-parameter bifurcation diagrams for $n:m$ phase-locking in a pair of thalamic neurons given varying levels of heterogeneity. All panels show the existence of fixed points in the $O(\varepsilon)$ reduction (red), $O(\varepsilon^2)$ reduction (blue), and full model (black). Solid (dashed) curves correspond to stable (unstable) fixed points.

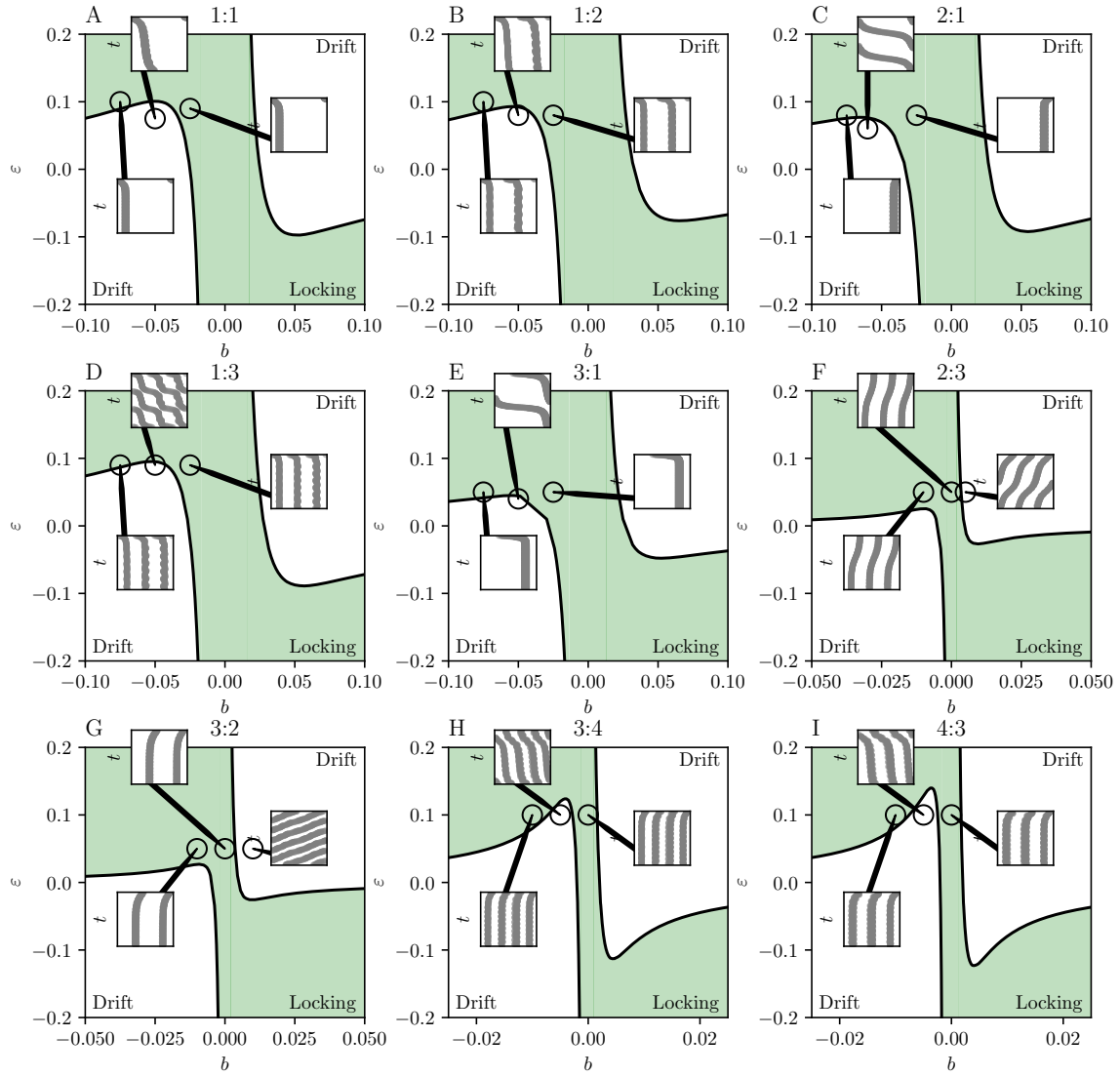


Figure 12: Two-parameter bifurcation diagrams of the reduced coupled thalamic model for $n:m$ phase-locking. The horizontal axis is the heterogeneity b and the vertical axis is the coupling strength ε .

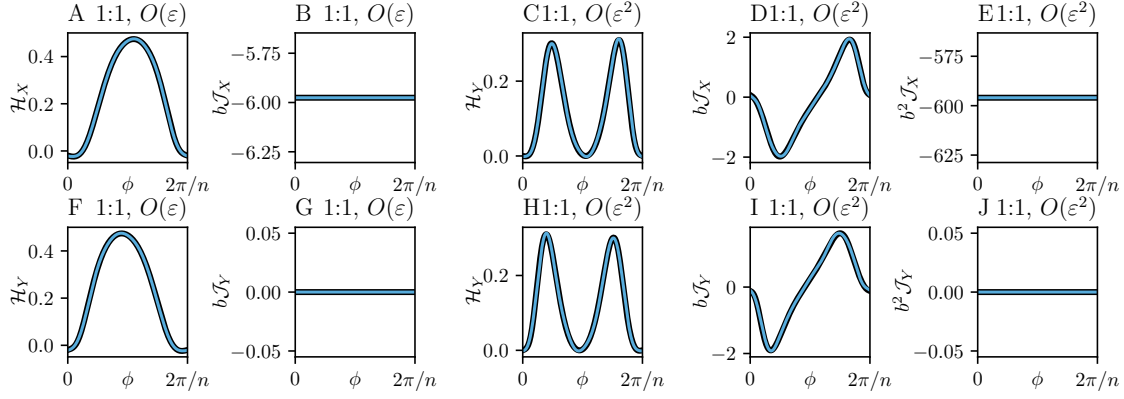


Figure 13: Original \mathcal{H} - and \mathcal{J} -functions (black) vs the corresponding Fourier approximation (blue) for 1:1 phase-locking.

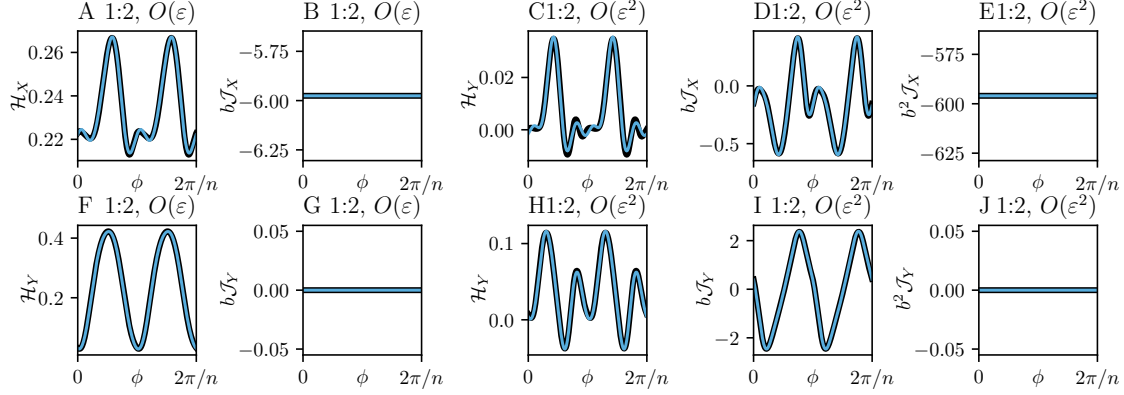


Figure 14: Original \mathcal{H} - and \mathcal{J} -functions (black) vs the corresponding Fourier approximation (blue) for 1:2 phase-locking.

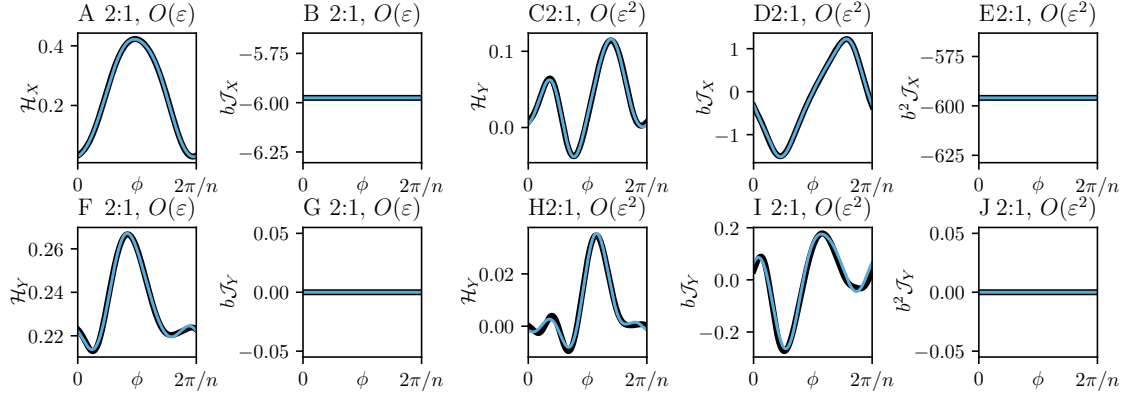


Figure 15: Original \mathcal{H} - and \mathcal{J} -functions (black) vs the corresponding Fourier approximation (blue) for 2:1 phase-locking.

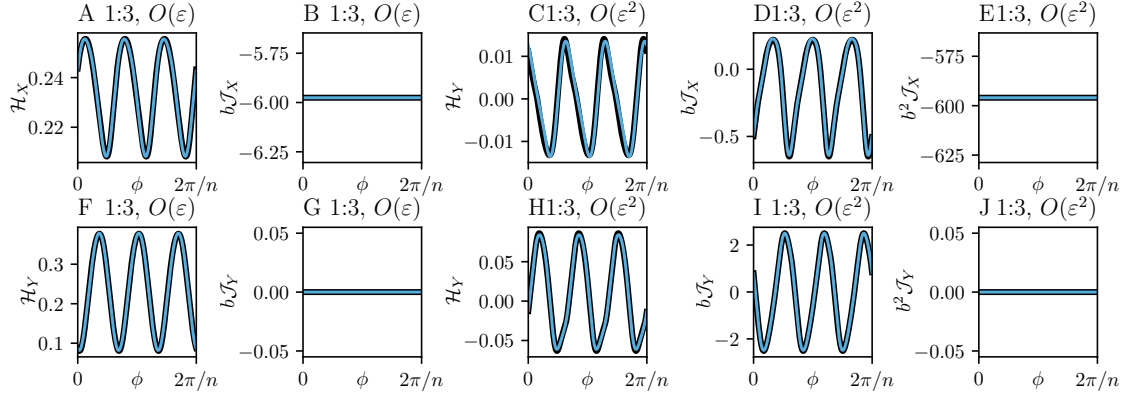


Figure 16: Original \mathcal{H} - and \mathcal{J} -functions (black) vs the corresponding Fourier approximation (blue) for 1:3 phase-locking.

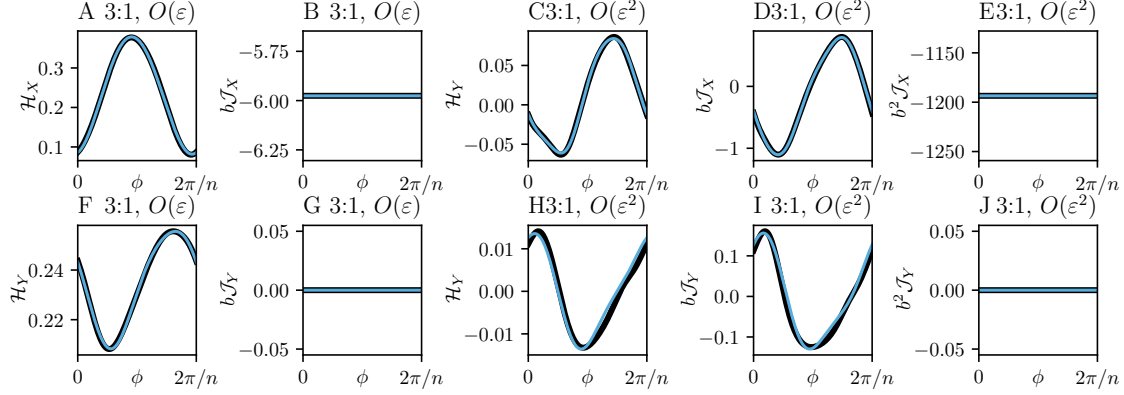


Figure 17: Original \mathcal{H} - and \mathcal{J} -functions (black) vs the corresponding Fourier approximation (blue) for 3:1 phase-locking.

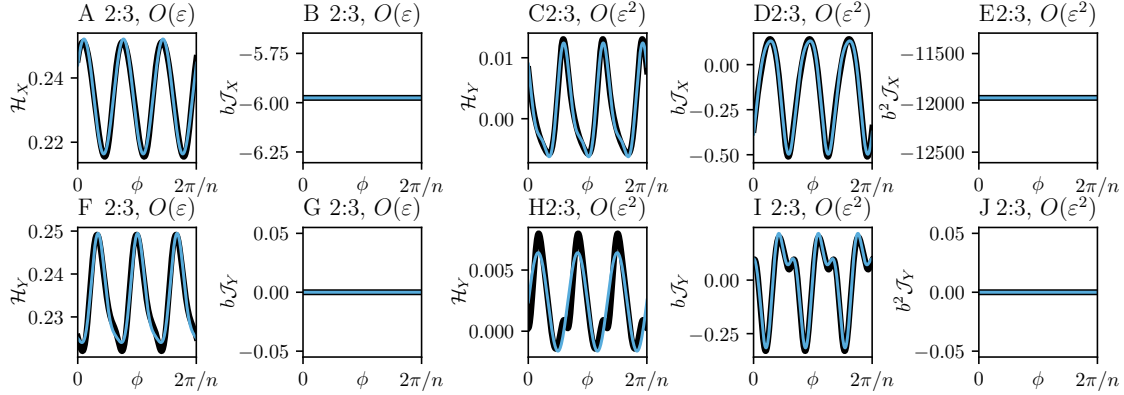


Figure 18: Original \mathcal{H} - and \mathcal{J} -functions (black) vs the corresponding Fourier approximation (blue) for 2:3 phase-locking.

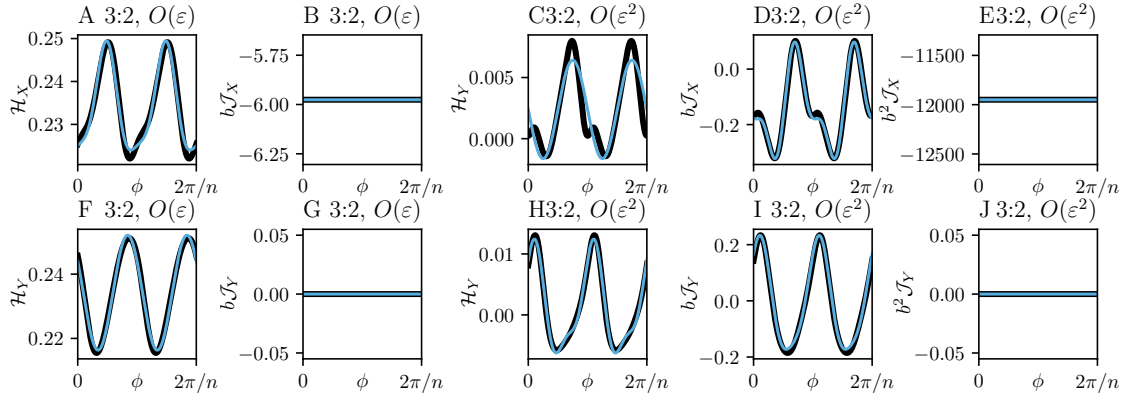


Figure 19: Original \mathcal{H} - and \mathcal{J} -functions (black) vs the corresponding Fourier approximation (blue) for 3:2 phase-locking.

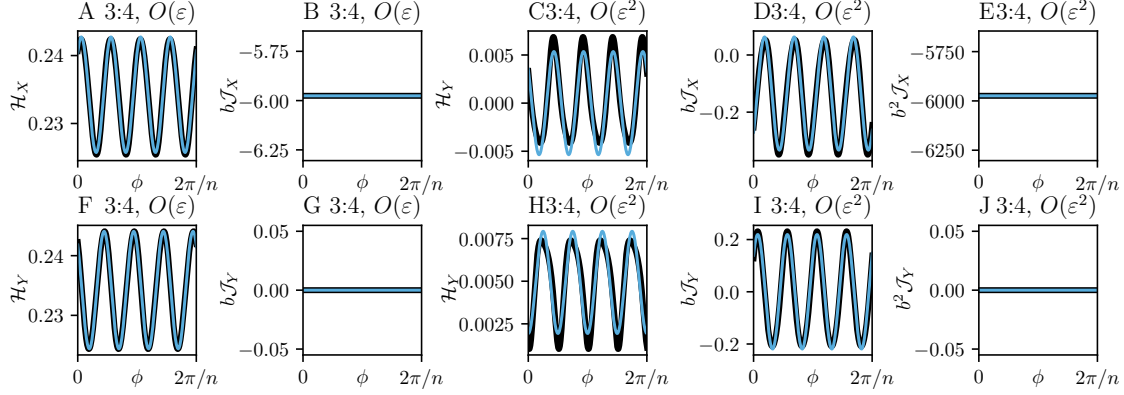


Figure 20: Original \mathcal{H} - and \mathcal{J} -functions (black) vs the corresponding Fourier approximation (blue) for 3:4 phase-locking.

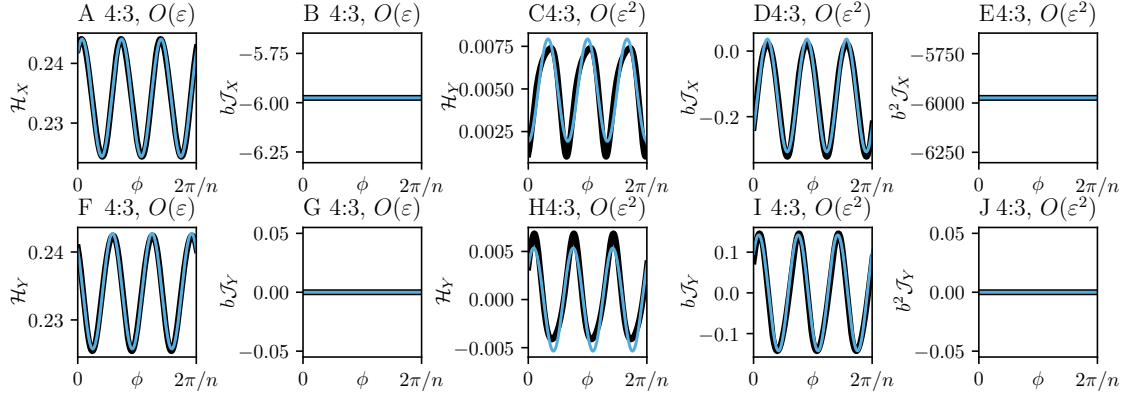


Figure 21: Original \mathcal{H} - and \mathcal{J} -functions (black) vs the corresponding Fourier approximation (blue) for 4:3 phase-locking.